https://doi.org/10.61092/iaea.qmtx-kyyh

INDC(NDS)-0631
Distr. FE

IAEA
International Atomic Energy Agency

INDC International Nuclear Data Committee

Benchmarking of the FENDL-3 Neutron Cross-Section Data Library for Fusion Applications

U. Fischer[(1)], M. Angelone[(2)], P. Batistoni[(2)], T. Bohm[(3)], K. Kondo [(1)], C. Konno[(4)], M. Sawan[(3)], R. Villari[(2)], B. Walker[(3)]

[(1)]Association KIT-Euratom, Karlsruhe Institute of Technology,
Hermann-von-Helmholtz-Platz 1, D 76344 Eggenstein-Leopoldshafen, Germany
[(2)]Associazione ENEA-Euratom, ENEA Fusion Division,
Via E. Fermi 27, I-00044 Frascati, Italy

[(3)]University of Wisconsin-Madison, 1500 Engineering Dr,
Madison, WI 53706, USA

[(4)]Japan Atomic Energy Agency, Tokai-mura, Naka-gun,
Ibaraki-ken 319-1195, Japan

March 2014

IAEA Nuclear Data Section
Vienna International Centre, P.O. Box 100, 1400 Vienna, Austria

Selected INDC documents may be downloaded in electronic form from
http://www-nds.iaea.org/publications
or sent as an e-mail attachment.
Requests for hardcopy or e-mail transmittal should be directed to
NDS.Contact-Point@iaea.org
or to:
Nuclear Data Section
International Atomic Energy Agency
Vienna International Centre
PO Box 100
1400 Vienna
Austria

Printed by the IAEA in Austria

March 2014

INDC(NDS)-0631

Distr. FE

Benchmarking of the FENDL-3 Neutron Cross Section Data Library for Fusion Applications

U. Fischer[(1)], M. Angelone[(2)], P. Batistoni[(2)], T. Bohm[(3)], K. Kondo [(1)], C. Konno[(4)], M. Sawan[(3)], R. Villari[(2)], B. Walker[(3)]

[(1)]Association KIT-Euratom, Karlsruhe Institute of Technology,
Hermann-von-Helmholtz-Platz 1, D 76344 Eggenstein-Leopoldshafen, Germany
[(2)]Associazione ENEA-Euratom, ENEA Fusion Division,
Via E. Fermi 27, I-00044 Frascati, Italy

[(3)]University of Wisconsin-Madison, 1500 Engineering Dr,
Madison, WI 53706, USA

[(4)]Japan Atomic Energy Agency, Tokai-mura, Naka-gun,
Ibaraki-ken 319-1195, Japan

ABSTRACT

This report summarizes the benchmark analyses performed in a joint effort of ENEA (Italy), JAEA (Japan), KIT (Germany), and the University of Wisconsin (USA) with the objective to test and qualify the neutron induced general purpose FENDL-3.0 data library for fusion applications. The benchmark approach consisted of two major steps including the analysis of a simple ITER-like computational benchmark, and a series of analyses of benchmark experiments conducted previously at the 14 MeV neutron generator facilities at ENEA Frascati, Italy (FNG) and JAEA, Tokai-mura, Japan (FNS).

The computational benchmark revealed a modest increase of the neutron flux levels in the deep penetration regions and a substantial increase of the gas production in steel components. The comparison to experimental results showed good agreement with no substantial differences between FENDL-3.0 and FENDL-2.1 for most of the responses analysed. There is a slight trend, however, for an increase of the fast neutron flux in the shielding experiment and a decrease in the breeder mock-up experiments. The photon flux spectra measured in the bulk shield and the tungsten experiments are significantly better reproduced with FENDL-3.0 data. In general, FENDL-3, as compared to FENDL-2.1, shows an improved performance for fusion neutronics applications. It is thus recommended to ITER to replace FENDL-2.1 as reference data library for neutronics calculation by FENDL-3.0.

March 2014

Table of Contents

1. Introduction

The International Fusion Evaluated Nuclear Data Library FENDL [1] has been developed under the auspices of the IAEA/NDS with the objective to provide a dedicated nuclear data library which satisfies the needs of fusion technology applications. Version FENDL-2.1 [2], assembled in 2004, serves as the current reference data library for ITER nuclear design analyses.

The recent Co-ordinated Research Project (CRP), organised by the IAEA/NDS [3] was dedicated to the creation of FENDL-3 as a major update and extension to FENDL-2.1. The related development step includes the updating of nuclear data evaluations from the major nuclear data projects such as ENDF/B, JEFF, JENDL and RUSFOND, the extension of the energy range of incident particles up to 150 MeV to comply with the requirements for design calculations of the accelerator based IFMIF neutron source, and the inclusion of full co-variance data to enable uncertainty assessments in design analyses.

The CRP has resulted in a starter library, called FENDL-3/SLIB, consisting of general purpose and activation sub-libraries with cross-section data for neutron, proton and deuteron induced reactions, as well as a neutron shadow library with full co-variance data. FENDL-3/SLIB, release 4 [4], is considered as final version of the library assuming its successful qualification by means of benchmark analyses.

This paper summarises the benchmark analyses performed in a joint effort of ENEA (Italy), JAEA (Japan), KIT (Germany), and the University of Wisconsin (USA) to test and qualify the neutron induced general purpose FENDL-3 data library for fusion applications.

2. FENDL-3/SLIB4 Neutron Data Library

The FENDL-3 starter library, version 4, includes 180 materials with general purpose evaluated data files for neutron transport calculations [6]. Applications libraries have been processed at the IAEA/NDS in the ACE format for Monte Carlo calculations and in the multi-group data format for deterministic calculations. The benchmark analyses reported in this paper are entirely based on Monte Carlo calculations performed with the MCNP code [7] and the ACE data files from the FENDL-3/SLIB4 library, here denoted as FENDL-3.0.

3. ITER Computational Benchmark

A suitable ITER relevant computational benchmark has been specified in the frame of previous FENDL benchmark efforts [8]. The benchmark builds on a one-dimensional model which replicates the radial build of the original ITER design in a simplified bulk geometry representation. Inboard and outboard systems are modelled as cylindrical rings with the plasma chamber in between and the torus axis as symmetry axis.

Fig. 1 illustrates schematically the radial build of the computational benchmark. The inboard (IB) and outboard (OB) components are modelled as cylindrical rings with the plasma in between. Fifteen million source neutrons were sampled from a uniform isotropic distribution in the plasma zone and normalized to 6.1 10^{17} $cm^{-2}s^{-1}$ yielding IB and OB neutron wall loadings of 1 and 1.5 MW/m^2, respectively. The calculations were performed with the MCNP code [10] using the ACE formatted processed nuclear data libraries. In these MCNP calculations, nuclear responses (flux, heating, radiation damage, and gas production) were compared using the FENDL-2.1 and the FENDL-3.0 libraries. This allows conclusions to be drawn on the impact of the new FENDL-3.0 data on ITER design calculations which are currently based on the FENDL-2.1 reference data library.

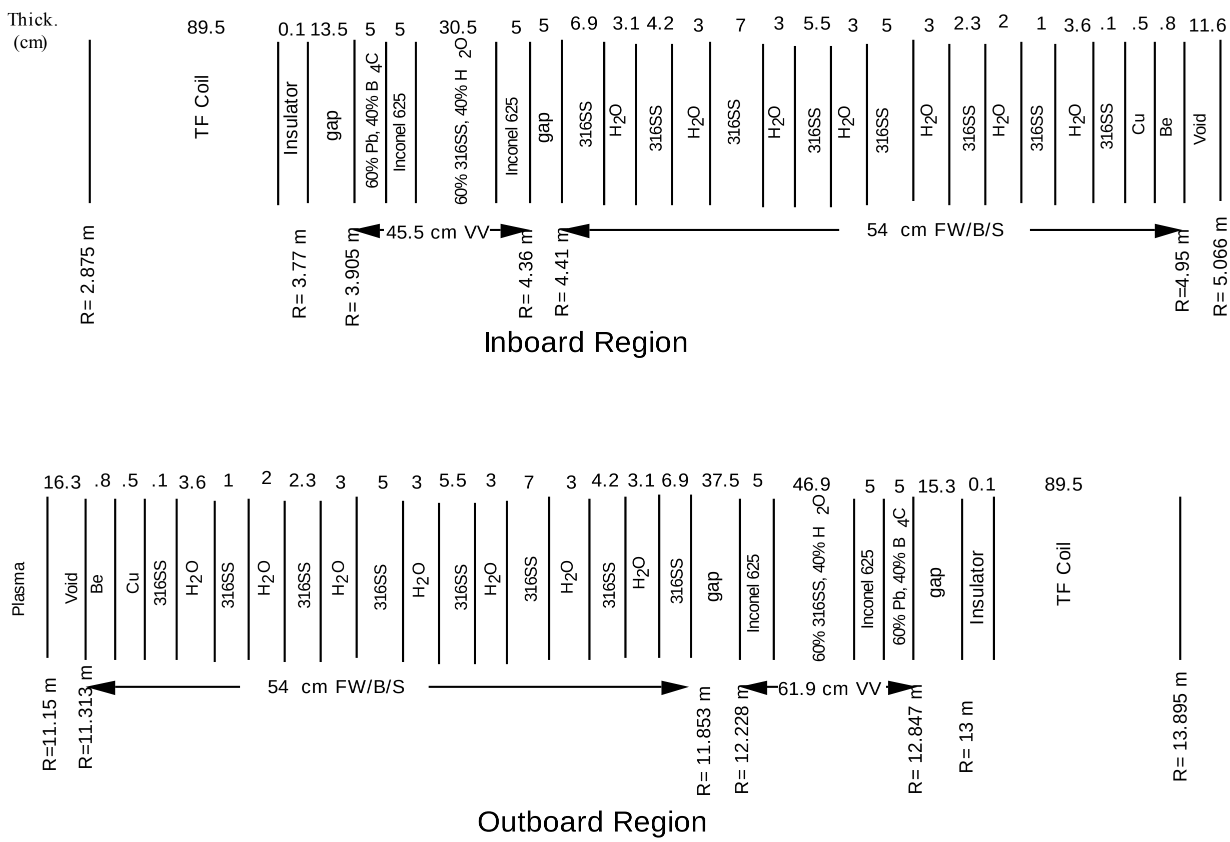

Fig. 1. Radial build of ITER calculational benchmark.

Neutron and Gamma Fluxes

Table I shows the peak neutron flux results with FENDL-3.0 compared to FENDL-2.1 in the different regions. The 1σ statistical uncertainties are also provided. There were noticeable changes in both the vacuum vessel (VV) and magnet. There was a 2.20% increase in the neutron flux in the IB VV, and a 2.74% increase in the neutron flux in the OB VV. The magnet saw a 4.06% increase in the IB region, and a 6.78% increase in the OB region. These results indicate that there is an increase of about 2.2-6.8% in the neutron flux in the components that are heavily shielded by water-cooled steel, such as the vacuum vessel and magnet, compared to FENDL-2.1.

TABLE I: PEAK NEUTRON FLUX RESULTS OBTAINED WITH FENDL-3.0 AND FENDL-2.1.

	FENDL-2.1		**FENDL-3.0**		% Change
	Neutron Flux	1 σ % Error	Neutron Flux	1 σ % Error	
IB					
FW					
Be	3.52E+14	0.05	3.51E+14	0.05	-0.03
Cu	3.09E+14	0.05	3.09E+14	0.05	-0.01
SS	2.96E+14	0.06	2.96E+14	0.06	0.01
VV	8.47E+11	0.19	8.66E+11	0.19	2.20
Magnet	3.37E+09	0.44	3.50E+09	0.44	4.06
OB					
FW					
Be	4.37E+14	0.03	4.37E+14	0.03	-0.05
Cu	3.95E+14	0.03	3.94E+14	0.03	-0.06
SS	3.80E+14	0.03	3.80E+14	0.03	-0.05
VV	1.17E+12	0.09	1.20E+12	0.09	2.74
Magnet	4.80E+08	0.41	5.12E+08	0.40	6.78

In Fig. 2, we show the neutron spectra at the front of the OB magnet for simulations using FENDL-3.0 and FENDL-2.1. From Fig. 2, the two spectra appear very similar. Fig. 3 shows a more detailed look at the difference in neutron spectra between FENDL-3.0 and FENDL-2.1. The neutron spectrum obtained using FENDL-3.0 is shown relative to that obtained using the FENDL-2.1 data as a function of energy. We see that there is approximately <10% increase in neutron flux at the front of the OB magnet for much of the energy regime with larger spikes (up to 20%) in the neutron flux difference in the high-energy region. The neutron spectrum behind the large volume of water-cooled steel is harder with FENDL-3.0. A notable change in FENDL-3.0 is the switch of H-1 data from JENDL-3.3 to ENDF/B-VII.0. Careful comparison of H-1 cross sections in the two libraries show lower (n,γ) cross sections at high energy in FENDL-3.0 that could be the reason for higher and harder neutron flux in regions heavily shielded by water-cooled steel.

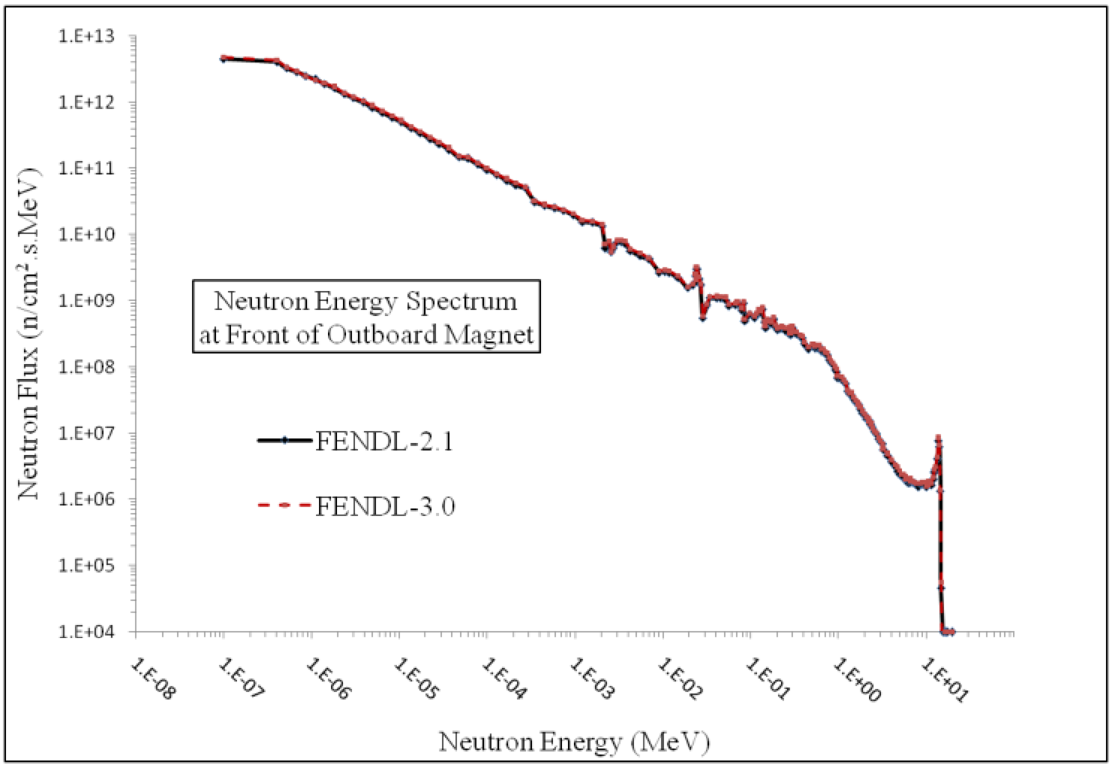

Fig. 2: Neutron flux spectra at the front of outboard magnet.

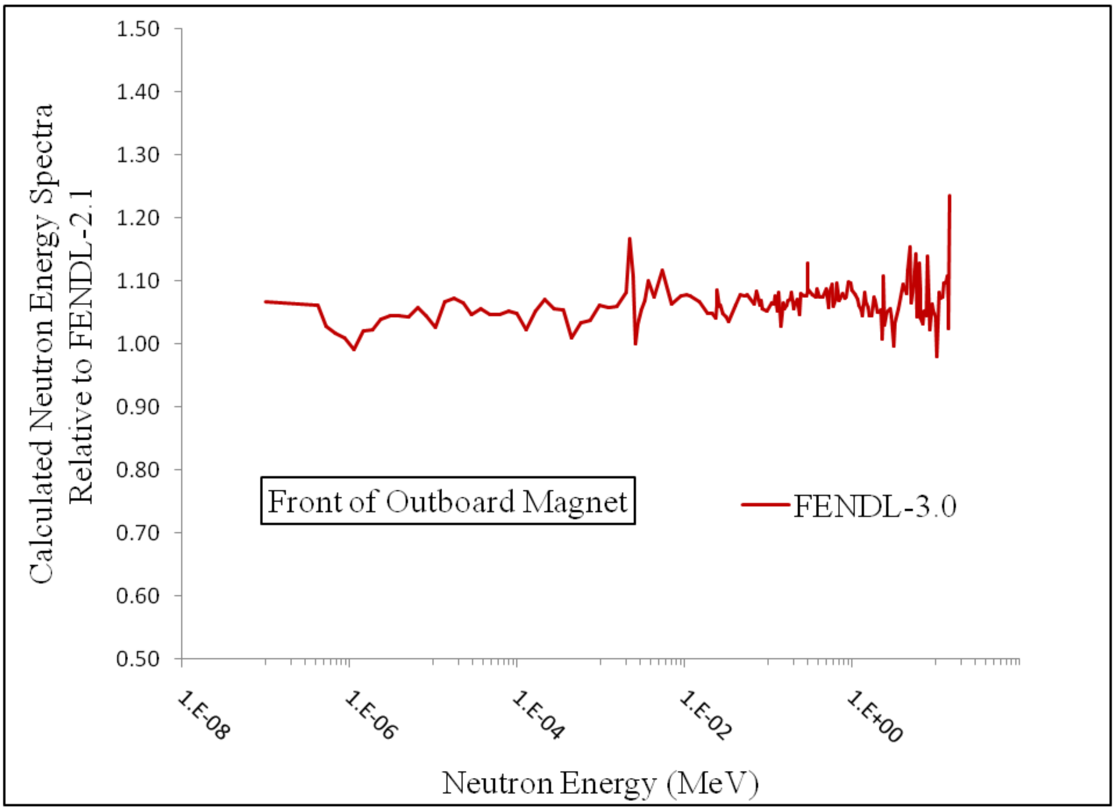

Fig. 3: Ratio of neutron flux spectra calculated with FENDL-3.0 and FENDL-2.1 at the front of the outboard magnet.

Table II shows the peak gamma flux results calculated with FENDL-3.0 and FENDL-2.1. As reported above, there were noticeable changes in both the VV and magnet neutron fluxes with increases in the range of 2-7%. The neutron energy spectrum was also slightly harder with FENDL-3.0 data at the inner surface of the magnet behind the large volume of water-cooled steel. On the other hand, the results for gamma flux in Table II show a modest change in the gamma flux with the largest being an increase of ~2% at the magnet.

TABLE II: PEAK GAMMA FLUX RESULTS OBTAINED WITH FENDL-3.0 AND FENDL-2.1.

	FENDL-2.1		**FENDL-3.0**		% Change
	Gamma Flux	1 σ % Error	Gamma Flux	1 σ % Error	
IB					
FW					
Be	3.177E+14	0.05	3.209E+14	0.05	1.00
Cu	3.074E+14	0.05	3.104E+14	0.05	0.98
SS	3.068E+14	0.06	3.099E+14	0.06	1.01
VV	4.859E+11	0.17	4.855E+11	0.17	-0.08
Magnet	1.428E+09	0.37	1.458E+09	0.37	2.09
OB					
FW					
Be	3.616E+14	0.04	3.641E+14	0.04	0.70
Cu	3.605E+14	0.04	3.633E+14	0.04	0.78
SS	3.659E+14	0.04	3.693E+14	0.04	0.92
VV	6.607E+11	0.08	6.623E+11	0.08	0.24
Magnet	2.071E+08	0.35	2.116E+08	0.35	2.21

Nuclear Heating

Table III shows the peak nuclear heating results obtained with FENDL-3.0 and FENDL-2.1. The harder and higher neutron flux in the VV and magnet results in higher neutron heating in these components. However, it should be noted that gamma heating in these components dominates the total nuclear heating with ~90% contribution. The modest change in the gamma flux compared to the increase in neutron flux results in moderate changes in nuclear heating. For example, the peak VV heating decreased by ~1%. This reflects an increase in neutron heating of ~16% combined with a decrease in gamma heating of ~3%. Nuclear heating in the magnet increases by only ~2% with neutron heating increasing by ~8% and gamma heating increasing by only ~0.7%.

TABLE III: PEAK POWER DENSITY [W/Cm^3] RESULTS

	FENDL-2.1		**FENDL-3.0**		
	Power Density	1 σ % Error	Power Density	1 σ % Error	% Change
IB					
FW					
Be	1.008E+01	0.05	1.007E+01	0.05	-0.06
Cu	2.017E+01	0.06	1.990E+01	0.07	-1.34
SS	1.785E+01	0.08	1.773E+01	0.08	-0.65
VV SS	2.635E-02	0.18	2.597E-02	0.18	-1.43
Magnet	5.422E-05	0.45	5.509E-05	0.45	1.60
OB					
FW					
Be	1.391E+01	0.03	1.390E+01	0.03	-0.07
Cu	2.476E+01	0.04	2.444E+01	0.05	-1.29
SS	2.230E+01	0.05	2.221E+01	0.05	-0.39
VV SS	3.576E-02	0.09	3.536E-02	0.09	-1.13
Magnet	7.800E-06	0.43	7.941E-06	0.43	1.81

Atomic Displacement Damage

Table IV compares the peak atomic displacement rates in the different regions obtained using the two libraries. Atomic displacement damage is higher in the VV and magnet with FENDL-3.0 due to the higher and harder neutron flux. The effect is more pronounced in the outboard magnet because of the thicker water-cooled steel in front of it.

TABLE IV: ATOMIC DISPLACEMENT RATE [dpa/fpy] RESULTS (fpy = full power year).

	FENDL-2.1		**FENDL-3.0**		
	dpa/fpy	1 σ % Error	dpa/fpy	1 σ % Error	% Change
IB					
FW					
Cu	9.165E+00	0.06	9.135E+00	0.06	-0.33
SS (Fe)	7.790E+00	0.07	7.784E+00	0.07	-0.08
VV					
Inconel (Ni)	1.016E-02	0.21	1.041E-02	0.21	2.52
SS (Fe)	3.368E-03	0.24	3.448E-03	0.24	2.37
Magnet (Cu)	3.898E-05	0.48	4.064E-05	0.48	4.27
OB					
FW					
Cu	1.377E+01	0.03	1.373E+01	0.03	-0.28
SS (Fe)	1.182E+01	0.03	1.182E+01	0.03	-0.02
VV					
Inconel (Ni)	1.382E-02	0.10	1.425E-02	0.10	3.11
SS (Fe)	5.021E-03	0.12	5.171E-03	0.12	2.98
Magnet (Cu)	5.627E-06	0.43	6.020E-06	0.42	6.99

Gas Production

Table V compares the peak helium production rates in the different regions obtained using the two libraries. Helium is produced by high-energy neutrons and is higher with FENDL-3.0 in the vacuum vessel and the magnet. An increase of ~18% e. g. is observed in the Inconel of the vacuum vessel with FENDL-3.0 data. This increase results from larger helium production cross sections in FENDL-3 at high energies for Ni and other SS constituents combined with the higher and harder neutron fluxes/spectra in the vacuum vessel and the magnet.

TABLE V: PEAK HELIUM PRODUCTION RATE [He appm/fpy] (appm = atomic parts per million; fpy = full power year).

	FENDL-2.1		**FENDL-3.0**		% Change
	He appm/fpy	1 σ % Error	He appm/fpy	1 σ % Error	
IB					
FW					
Be	4.100E+03	0.07	4.103E+03	0.07	0.06
CuBeNi	2.103E+02	0.07	2.111E+02	0.07	0.38
SS316	1.773E+02	0.06	1.847E+02	0.06	4.21
VV					
Inconel	6.811E-02	0.32	7.995E-02	0.31	17.37
SS316	7.659E-02	0.22	8.249E-02	0.22	7.70
Magnet (Cu)	3.819E-04	0.62	4.020E-04	0.61	5.27
OB					
FW					
Be	5.981E+03	0.03	5.984E+03	0.03	0.05
CuBeNi	3.233E+02	0.03	3.248E+02	0.03	0.48
SS316	2.454E+02	0.03	2.561E+02	0.03	4.36
VV					
Inconel	9.042E-02	0.16	1.069E-01	0.16	18.28
SS316	1.076E-01	0.11	1.164E-01	0.11	8.19
Magnet (Cu)	5.570E-05	0.57	6.002E-05	0.56	7.75

Table VI compares the peak hydrogen production rates in the different regions obtained using the two libraries. Hydrogen is also produced by high-energy neutrons and the production rate is again higher with FENDL-3.0 in the vacuum vessel and the magnet. The increase is less pronounced than for the helium production due to the lower threshold energy for the H production reactions. The effect in Inconel is much lower than for He production.

TABLE VI: PEAK HYDROGEN PRODUCTION RATE [H appm/fpy] (appm = atomic parts per million; fpy = full power year).

	FENDL-2.1		**FENDL-3.0**		% Change
	H appm/fpy	1 σ % Error	H appm/fpy	1 σ % Error	
IB					
FW					
Be	6.103E+01	0.07	6.106E+01	0.07	0.05
CuBeNi	6.463E+02	0.07	6.461E+02	0.07	-0.03
SS316	6.020E+02	0.08	5.950E+02	0.08	-1.16
VV					
Inconel	5.762E-01	0.30	5.783E-01	0.30	0.37
SS316	1.170E-01	0.35	1.196E-01	0.34	2.16
Magnet (Cu)	1.080E-03	0.65	1.135E-03	0.64	5.07
OB					
FW					
Be	8.968E+01	0.03	8.968E+01	0.03	0.01
CuBeNi	9.994E+02	0.03	1.000E+03	0.03	0.06
SS316	9.414E+02	0.03	9.307E+02	0.03	-1.14
VV					
Inconel	7.670E-01	0.15	7.757E-01	0.15	1.14
SS316	1.677E-01	0.17	1.731E-01	0.17	3.18
Magnet (Cu)	1.566E-04	0.61	1.684E-04	0.60	7.50

Table VII compares the peak tritium production rates in the different regions obtained using the two libraries. Tritium production is also higher with FENDL-3.0 in the vacuum vessel and the magnet. An extremely large increase of more than a factor of two is observed for the Inconel in the vacuum vessel. Although T production is included in the H production it does not affect the value of the total H production due to its very small magnitude.

TABLE VII: PEAK TRITIUM PRODUCTION RATE [T appm/fpy] (appm = atomic parts per million; fpy = full power year).

	FENDL-2.1		FENDL-3.0		% Change
	T appm/fpy	1 σ % Error	T appm/fpy	1 σ % Error	
IB					
FW					
Be	6.101E+01	0.07	6.104E+01	0.07	0.05
CuBeNi	1.564E+00	0.07	1.563E+00	0.07	-0.04
SS316	1.196E-01	0.08	1.203E-01	0.08	0.63
VV					
Inconel	2.951E-06	0.52	6.922E-06	0.45	134.54
SS316	2.487E-05	0.36	2.546E-05	0.36	2.37
Magnet (Cu)	1.354E-06	0.87	1.431E-06	0.85	5.67
OB					
FW					
Be	8.964E+01	0.03	8.965E+01	0.03	0.01
CuBeNi	2.447E+00	0.03	2.448E+00	0.03	0.04
SS316	1.869E-01	0.04	1.882E-01	0.04	0.73
VV					
Inconel	3.782E-06	0.26	9.027E-06	0.23	138.66
SS316	3.574E-05	0.18	3.695E-05	0.18	3.37
Magnet (Cu)	1.825E-07	0.86	1.982E-07	0.84	8.62

The large helium and tritium production in Inconel when using FENDL-3.0 prompted a more detailed investigation. Hydrogen, helium, and tritium production rates in the front of the inboard Inconel vacuum vessel increased by 0.37%, 17.37% and 134.54%, respectively. We ran numerous test simulations and concluded that there is no single isotope in Inconel that can be pinpointed for causing all the excess production rates. Some of the FENDL-3.0 evaluations raised the production rates, while others lowered them. Careful examination of reaction rates for gas production indicated that the differences are due to large differences in missing reactions in the two FENDL libraries. We compared all the missing reactions in the ACE formatted processed data files for FENDL-2.1, FENDL-3.0, and ENDF/B-VII.0. These include D production (MT=204), T production (MT=205), and ^{3}He production (MT=206). We found that ENDF/B-VII.0 has the most missing reactions and FENDL-3.0 has the least. With respect to Inconel, there is a difference in missing reaction status for every major constituent isotope when comparing FENDL-2.1 to FENDL-3.0. Additionally, we specifically examined Al-27 because this isotope had a particularly large effect on the T production in Inconel. Including only the FENDL-3.0 evaluation of Al-27 caused the T production in the front of the outboard Inconel vacuum vessel to be more than double the FENDL-2.1 results. T production reaction (MT=205) was missing in FENDL-2.1, but present in FENDL-3.0. Using all ENDF/B-VII.0 data yielded a T production in the Inconel vacuum vessel that was very similar to that found with FENDL-3.0. Not surprisingly, reaction MT=205 is present in ENDF/B-VII.0. We conclude that it is very important that the processed ACE formatted data for FENDL-3.0 include all necessary reactions used for gas production by adding the missing reactions (MT=204, 205, and 206). This is of particular importance for analysis of fusion systems where neutrons are more energetic than in fission systems and tritium production and permeation has to be determined accurately for its environmental impact.

Magnet Nuclear Parameters

The superconducting magnet nuclear parameters are usually the design drivers for the shield in ITER and other magnetic confinement fusion systems. Hence, it is essential to accurately determine these parameters. Table VIII compares the peak nuclear parameters in the IB magnet that is less shielded than the OB leg of the TF magnet. The nuclear parameters in the magnet are higher by ~1.6-4.4% than predicted by FENDL-2.1. The largest effect is on the fast neutron fluence due to the harder and larger neutron flux. Similar increase is observed for Cu stabilizer dpa which is produced primarily by high energy neutrons. The increase in insulator absorbed dose and winding pack nuclear heating is smaller due to the contribution of gamma heating. Notice that the increase is much smaller for the magnet winding pack with ~90% contribution from gamma heating. Larger increase is observed for the insulator dose where light elements are used with only ~50% gamma heating contribution. Since magnet heating is the primary magnet shielding design driver in ITER, we conclude that switching to FENDL-3.0 is not urgently needed for ITER nuclear analysis.

TABLE VIII: PEAK INBOARD (IB) MAGNET RADIATION PARAMETERS
(gy = gray n; fpy = full power year).

	FENDL-2.1		FENDL-3.0		% change
	Value	1 σ % error	Value	1 σ % error	
Fast fluence (n/cm^2/fpy)	6.208E+16	0.45	6.480E+16	0.45	4.38
Insulator dose (Gy/fpy)	6.859E+05	0.43	7.091E+05	0.43	3.38
Cu dpa/fpy	3.898E-05	0.48	4.064E-05	0.48	4.27
Heating (mW/cm^3)	5.422E-02	0.40	5.509E-02	0.40	1.60

Conclusions of the Computational Benchmark Results

The results of the computational ITER-like benchmark indicate that using FENDL-3.0 yields higher and harder neutron flux/spectra in components that are heavily shielded by water-cooled steel, such as the vacuum vessel and magnet, compared to FENDL-2.1. However, the gamma flux has very modest change. This leads to only ~2% increase in the magnet heating which is the primary magnet shielding design driver in ITER. We observed large differences in the gas production results when using the two libraries. This was attributed to missing reactions in the processed FENDL libraries. It is very important that the processed ACE formatted data for FENDL-3.0 include all necessary reactions used for gas production by adding the missing reactions. This is of particular importance for analysis of fusion systems where neutrons are more energetic than in fission systems yielding significant gas production that impacts structural material integrity. In addition, tritium production and permeation has to be determined accurately due to its environmental impact.

The superconducting magnet nuclear parameters are usually the design drivers for the shield in ITER and other magnetic confinement fusion systems. Hence, it is essential to accurately determine these parameters. Table VIII compares the peak nuclear parameters in the IB magnet that is less shielded than the OB leg of the TF magnet. The nuclear parameters in the magnet are higher by ~1.6-4.4% than predicted by FENDL-2.1. The largest effect is on the fast neutron fluence due to the harder and larger neutron flux. Similar increase is observed for Cu stabilizer dpa which is produced primarily by high energy neutrons. The increase in insulator absorbed dose and winding pack nuclear heating is smaller due to the contribution of gamma heating. Notice that the increase is much smaller for the magnet winding pack with ~90% contribution from gamma heating. Larger increase is observed for the insulator dose where light elements are used with only ~50% gamma heating contribution.

4. Experimental Fusion Neutronics Benchmarks

A series of fusion relevant 14 MeV neutron experiments has been conducted over the past decades which are suitable for the benchmarking of fusion nuclear data. These include neutron transmission experiments on pure material assemblies with measurements of neutron spectra and specific reaction rates using activation foils, and so-called design oriented benchmark experiments on neutronic mock-ups of blanket and/or shield assemblies. A selected set of the most relevant experiments, conducted previously at the Fusion Neutron Source (FNS) of the Japanese Atomic Energy Agency (JAEA) at Tokai-mura, Japan, and the Frascati Neutron Generator (FNG) of ENEA, Italy, was used for benchmarking the FENDL-3.0 data library against experimental results. Most of these experiments are documented in the SINBAD compilation [9].

4.1 FNS Benchmark Experiments

Many integral benchmark experiments with DT neutrons have been carried out for nuclear data validation purposes at the FNS facility of JAEA since 1981. An overview of the experiments performed through the 1980 – 90 decades is given in Ref. [10].

Three types of integral benchmark experiments have been performed at FNS/JAEA: (1) in situ benchmark experiments, (2) Time-of-flight (ToF) experiment, and (3) design-oriented breeding blanket experiments. The first and second types of experiments were conducted for the benchmarking of nuclear data and were thus used for the FENDL-3 benchmark analysis presented in this report.

(1) "In situ" benchmark experiments [11]

Fig. 4 shows a typical experimental configuration as used in the "in situ" benchmark experiments at FNS. Neutron spectra over almost the whole neutron energy, reaction rates for various reactions, gamma heating rates, etc. were measured inside the experimental assembly of a simple geometrical assembly. The size of the experimental assemblies is different for each experiment depending on the amount of material available in each case. Experimental data from such experiments are available for lithium oxide, beryllium, graphite, silicon carbide, vanadium, iron, type 316 stainless steel (SS316), copper, tungsten, and others.

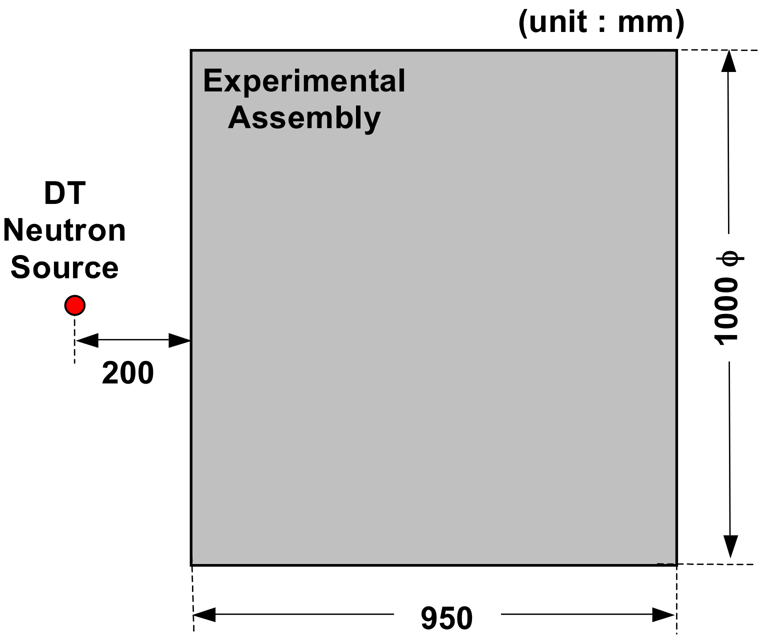

Fig. 4: Schematic set-up of the FNS "in-situ" experiments.

(2) Time-of-Flight (ToF) experiments [12]

Fig.5 shows a typical configuration as used for the ToF-experiments at FNS. In these experiments, neutron leakage spectra from 100 keV to 15 MeV have been measured at various angles. The material assemblies consisted of simple cylindrical slabs. Angular neutron leakage spectra were measured for lithium oxide, beryllium, graphite, nitrogen, oxygen, iron, copper, lead, and others employing a collimator system. The size of the material assemblies was different for each experiment depending on the amount of material which was available in each case.

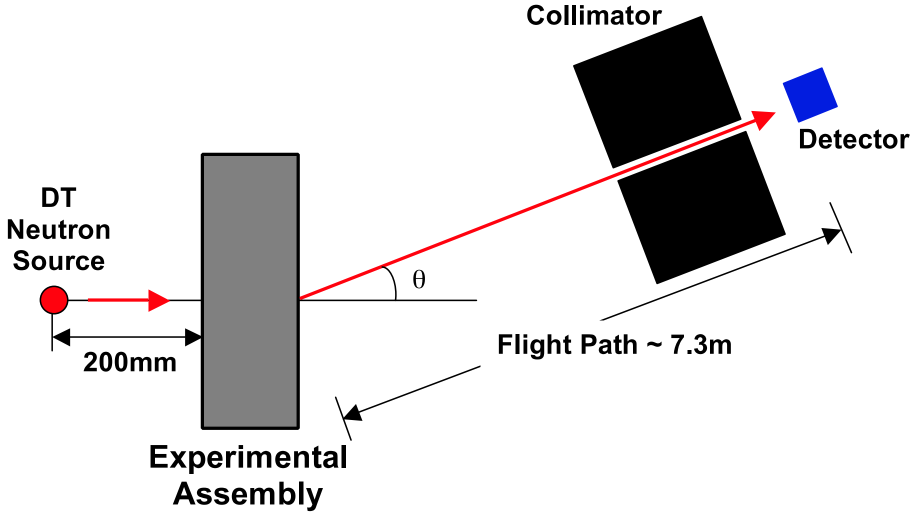

Fig. 5: Schematic set-up of the FNS Time-of-Flight (ToF) experiments.

Table IX lists all experimental configurations analysed for the FENDL-3 benchmarking and summarizes the results obtained in each case. Some specific configurations are shown in Figs. 6 to 9 for the material assemblies used in the ToF-experiments, and the "in-situ" experiments on SiC, V and SS-316. All calculations were performed with the MCNP5 Monte Carlo code [7] using the nuclear data libraries FENDL-2.1, FENDL-3/SLIB4, and, for comparison, the latest version of the Japanese Nuclear Data Library JENDL-4.0 [12]. Graphical results are displayed in Figs. 10-25. A brief discussion of the results is included in Table IX.

TABLE IX: SUMMARY OF FNS BENCHMARK EXPERIMENTS – MATERIAL CONFIGURATIONS AND DISCUSSION OF RESULTS.

Experiment		Assembly		Results discussion
		Shape	Size	
Li_2O	in situ	Quasi cylinder as shown in Fig. 6	630 mm effective diameter 610 mm thickness	All calculation results are almost identical and agree with the measured data well within the experimental error except for the reaction rate of the ^{27}Al(n,α)^{24}Na reaction and the fission rate of ^{235}U, C/Es of which are outside the experimental errors but are considered to be good.
	ToF	Quasi cylinder as shown in Fig. 6	630 mm in effective diameter 48, 200, 400 mm in thickness	All calculations reproduce the measured leakage neutron spectra from the lithium oxide slabs very well.
Be	in situ	Quasi cylinder as shown in Fig. 6	630 mm in effective diameter 455 mm in thickness	The calculations with FENDL-3/SLIB4 slightly improve the large discrepancy between the calculated and measured reaction rates of the ^{6}Li(n,α)^{3}T, ^{197}Au(n,γ)^{198}Au and ^{235}U(n,fission) reactions, which are sensitive to low energy neutrons. JENDL-4.0 shows larger discrepancies.
	ToF	Quasi cylinder as shown in Fig. 6	630 mm in effective diameter 51, 152 mm in thickness	All calculations reproduce the measured leakage neutron spectra from the beryllium slabs very well.
C (Graphite)	in situ	Quasi cylinder as shown in Fig. 6	630 mm in effective diameter 610 mm in thickness	All calculation results are almost identical and agree with the measured data well within the experimental error or slightly over the experimental error.
	ToF	Quasi cylinder as shown in fig. 6	630 mm in effective diameter 51, 202, 405 mm in thickness	All calculations reproduce the measured leakage neutron spectra from the graphite slabs very well.
Liq. N_2	ToF	Cylinder tank	600 mm in diameter 200 mm in thickness	All calculation results agree well with the measured neutron flux spectra except for the angle 66.6 deg.
Liq. O_2	ToF	Cylinder tank	600 mm in diameter 200 mm in thickness	All calculations underestimate the neutron flux spectra at larger angles.
SiC	in situ	Rectangular as shown in Fig. 7	457 mm x 457 mm x 711 mm in thickness	The calculations with FENDL-2.0 and -3/SLIB underestimate the measured reaction rates of the ^{93}Nb(n,2n)^{92m}Nb, ^{27}Al(n,α)^{24}Na and ^{115}In(n,n')^{115m}In reactions with increasing depth while JENDL-4.0 gives better agreement. The calculations with FENDL-3/SLIB agrees best with the measured reaction rate of the ^{197}Au(n,γ)^{198}Au reaction. The measured

				gamma ray heating rate is not well reproduced by the calculations with all libraries.
V	in situ	Rectangular as shown in Fig. 8	254 mm x 254 mm x 254 mm in thickness covered with 50 mm thick graphite	The vanadium data in FENDL-3/SLIB come from JENDL-4.0. The calculations with FENDL-3/SLIB and JENDL-4.0 agree well with the measured reaction rates of the ^{93}Nb(n,2n)^{92m}Nb and ^{115}In(n,n')^{115m}In reactions though the agreement for the ^{115}In(n,n')^{115m}In reaction is slightly worse with FENDL-2.1. All the calculations largely underestimate the measured data for low energy neutrons.
Fe	in situ	Cylinder	1000 mm in diameter 950 mm in thickness	All calculations agree with the measurements within 15%. There is a different C/E trend, however, for the calculations results with the FENDL data and JENDL-4.0. The C/E of the neutron flux above 10 MeV tends to decrease with increasing depth in the FENDL calculations while it tends to increase with increasing depth in the calculations with JENDL-4.0. The C/E ratio of the reaction rates for the ^{115}In(n,n')^{115m}In reaction tends to increase with increasing depth in the FENDL calculations while it tends to be almost flat for the JENDL-4.0 calculations. The difference of the C/E ratios for the neutron flux from 10 eV to 100 eV between the FENDL and the JENDL-4.0 calculations is at maximum 15 %. The gamma heating rate calculated with the FENDL data agrees better with the measurements than JENDL-4.0.
	ToF	Cylinder	1000 mm in diameter 50, 200, 400, 600 mm in thickness	For the 50 and 200 mm thick iron assemblies, all calculations reproduce the measured leakage neutron spectra above 100 keV very well. For the 400 and 600 mm thick iron assemblies, there is less good agreement with the measured leakage neutron spectra below 1 MeV.
SS-316	in situ	Cylinder with reflector as shown in Fig. 9	1200 mm in diameter 1118 mm in thickness	All calculations agree with the measured neutron flux above a few hundred eV while they overestimate the measured neutron flux below a few hundred eV. It is also noted that the calculation results obtained with FENDL-3/SLIB above 1 MeV tend to be larger at the deeper positions than those obtained with FENDL-2.1 and JENDL-4.0.
Cu	in situ	Quasi cylinder as shown in Fig. 6	630 mm in effective diameter 610 mm in thickness	All calculations give almost the same results although JENDL-4.0 data result in larger ^{93}Nb(n,2n)^{92m}Nb reaction rates with increasing depth than the FENDL data. The C/E ratios for ^{115}In(n,n')^{115m}In the reaction rate are within 15% up to the depth of 400 mm while all the calculations overestimate this reaction rate by more than 25% at the depth of 500 mm. The C/E ratios of the integrated neutron flux from 0.1 to 1 MeV largely change at every position. All calculations underestimate the measured neutron flux below 600 eV. It is considered that all nuclear data evaluations show deficiencies.
W	in situ	Quasi cylinder as shown in Fig. 6	575 mm in effective diameter 507 mm in thickness	All calculations slightly overestimate the measured ^{93}Nb(n,2n)^{92m}Nb reaction rate at positions deeper than 200 mm. They also agree with the measured reaction rate of the ^{115}In(n,n')^{115m}In reaction within 15%. However, the calculations underestimate the measured ^{186}W(n,γ)^{187}W reaction rate by more than 20% at the depth of 380 mm. All calculated gamma ray heating rates agree with the measurement within the (large) experimental error.
Pb	ToF	Quasi cylinder as shown in Fig. 6	100 cm in diameter 51, 203, 406 mm in thickness	All calculations generally agree very well with the measured neutron leakage flux spectra with the exception of JENDL-4.0 which, at the neutron energy around 10 MeV, produces a smaller peak than the measured one.

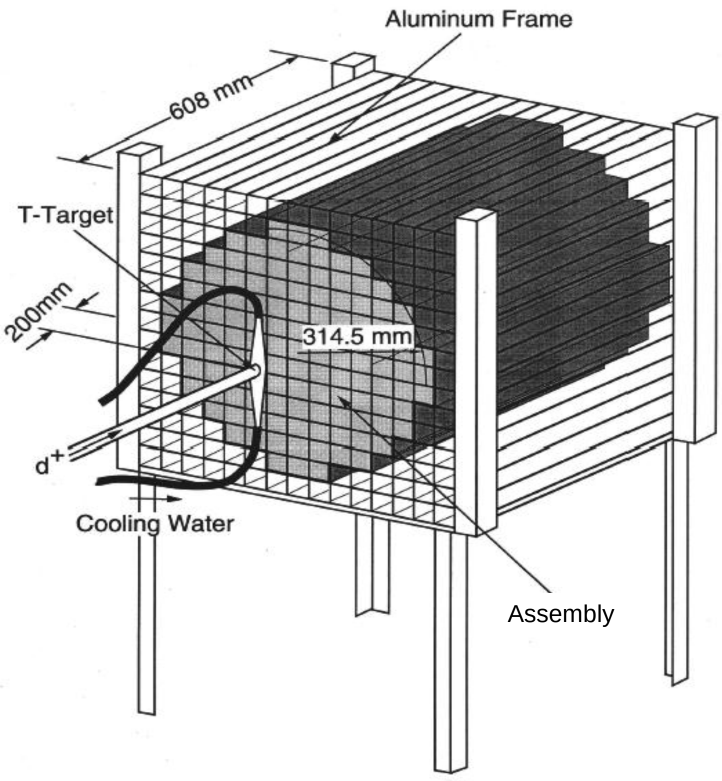

Fig. 6: Quasi cylindrical material assembly used in ToF and some "in-situ" FNS experiments.

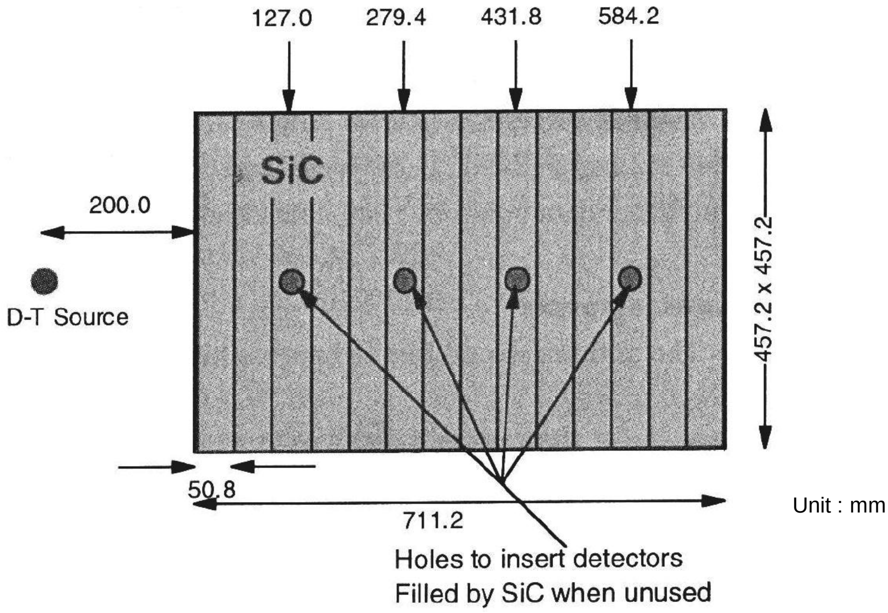

Fig. 7: Schematic set-up of the SiC in-situ experiment at FNS.

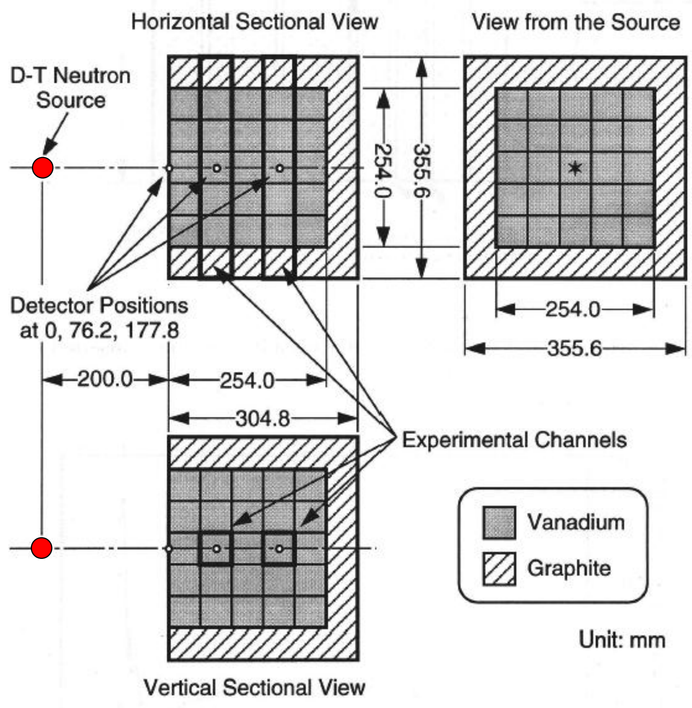

Fig. 8: Schematic set-up of the V in-situ experiment at FNS.

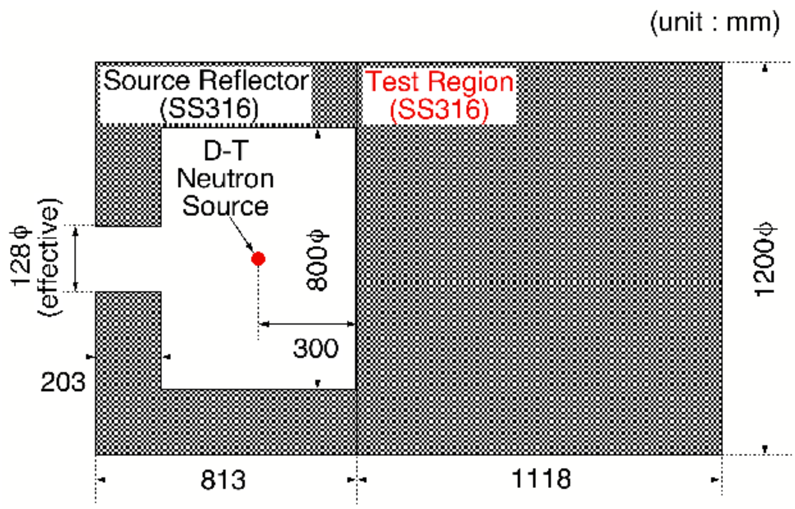

Fig. 9: Schematic set-up of the SS-316 in-situ experiment at FNS.

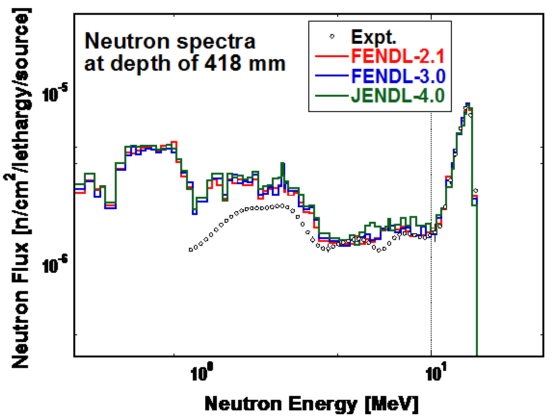

Fig. 10a Neutron spectra at 418 mm in Li_2O *in situ* experiment.

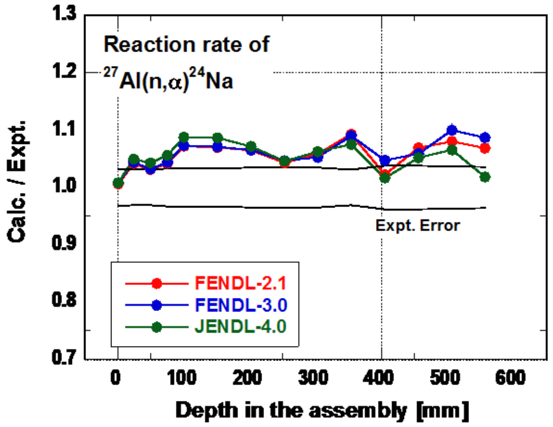

Fig. 10b Ratios of calculation to experiment for reaction rate of $^{27}Al(n,\alpha)^{24}Na$ in Li_2O *in situ* experiment.

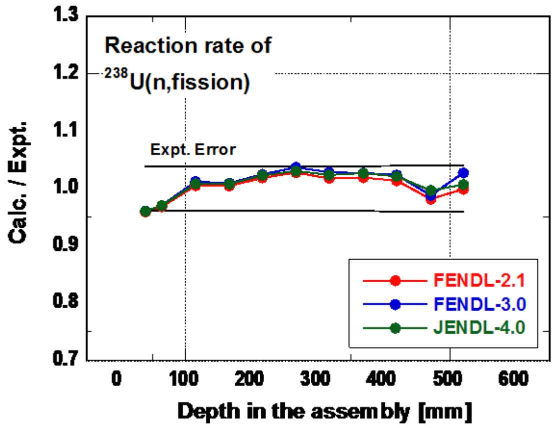

Fig. 10c Ratios of calculation to experiment for ^{238}U fission rate in Li_2O *in situ* experiment.

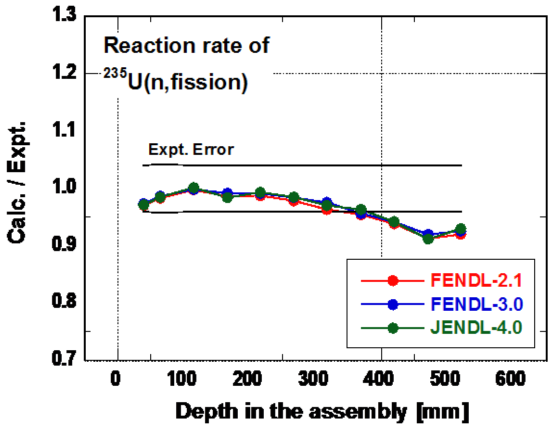

Fig. 10d. Ratios of calculation to experiment for ^{235}U fission rate in Li_2O *in situ* experiment.

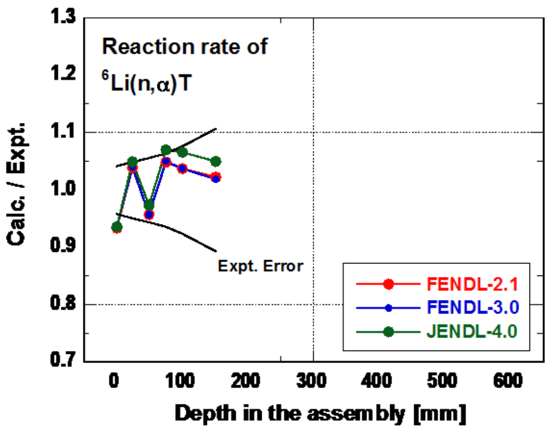

Fig. 10e. Ratios of calculation to experiment for reaction rate of $^{7}Li(n,n'\alpha)^{3}T$ in Li_2O *in situ* experiment.

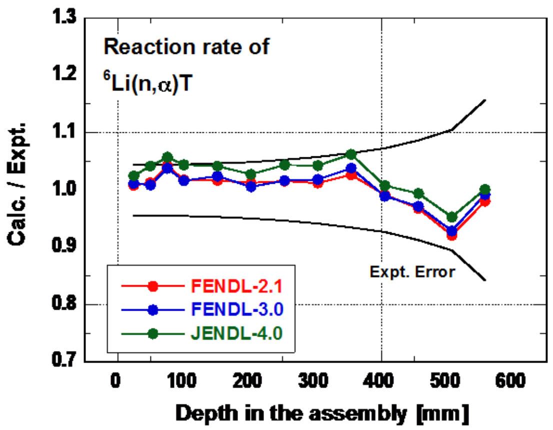

Fig. 10f Ratios of calculation to experiment for reaction rate of $^{6}Li(n,\alpha)^{3}T$ in Li_2O *in situ* experiment.

Fig. 10: Results obtained for the Li_2O in-situ experiment at FNS showing neutron flux spectra and C/E ratios for measured reaction rates.

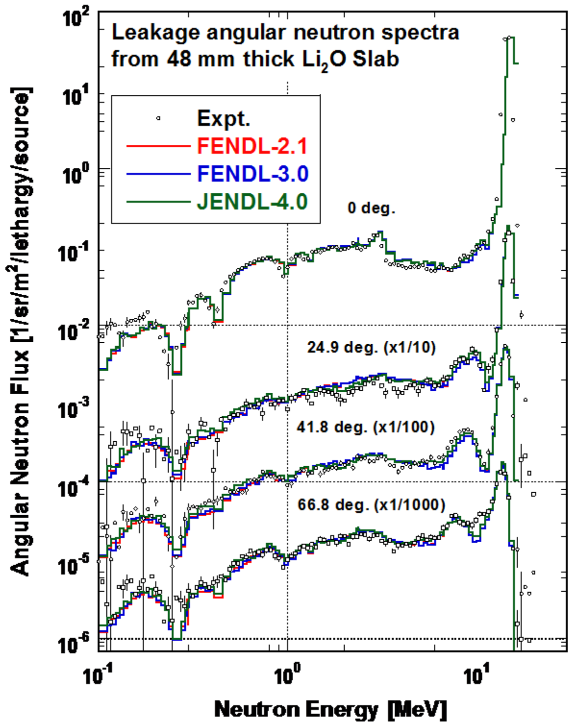

Fig. 11a: Angular neutron leakage spectra from 48 mm thick Li_2O slab.

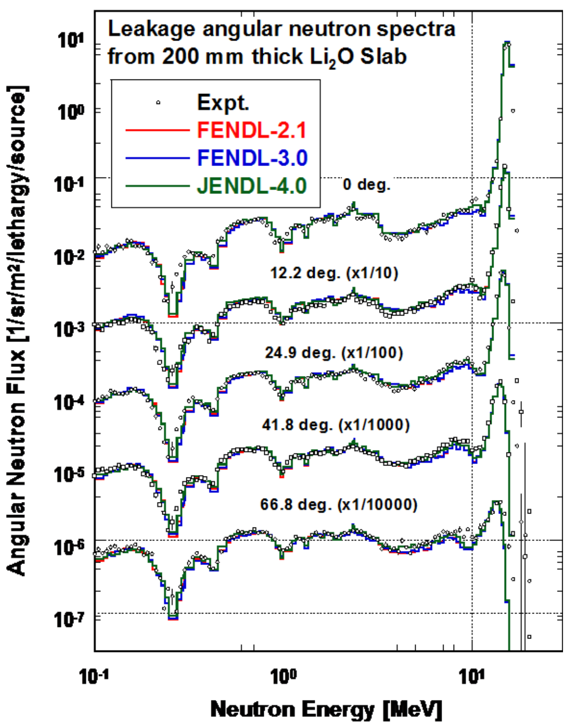

Fig. 11b: Angular neutron leakage spectra from 200 mm thick Li_2O.

Fig. 11: Results obtained for the Li_2O ToF-experiment at FNS showing angular neutron leakage spectra for 48 and 200 mm thick slabs.

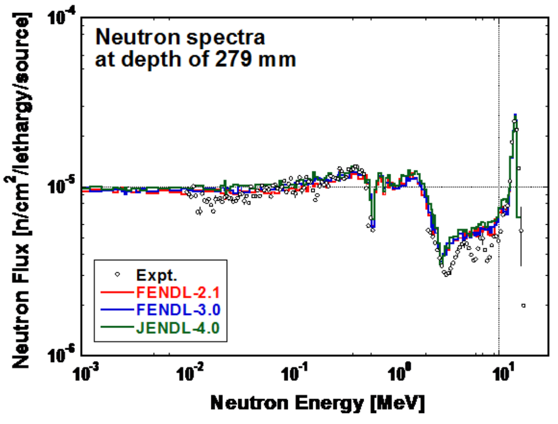

Fig. 12a: Neutron spectra at 279 mm in Be *in situ* experiment.

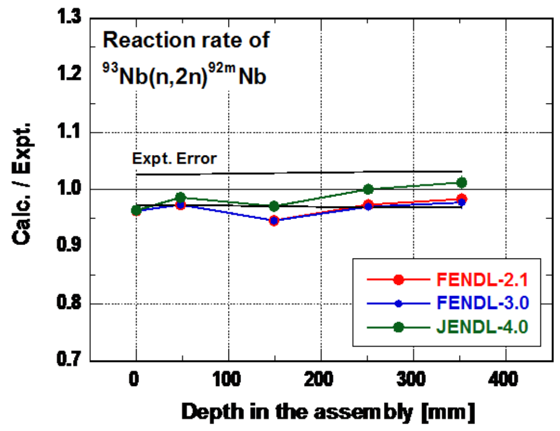

Fig. 12b: Ratios of calculation to experiment for reaction rate of ^{93}Nb(n,2n)^{92m}Nb in Be *in situ* experiment

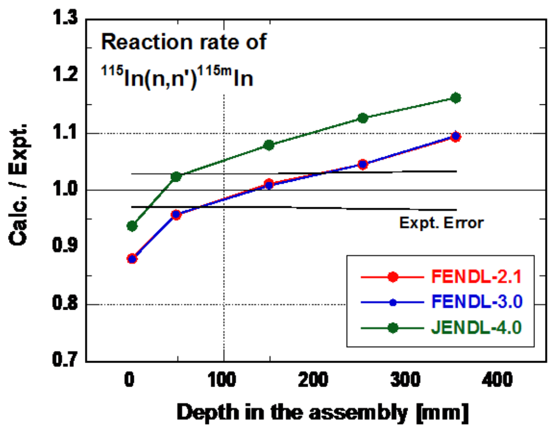

Fig. 12c: Ratios of calculation to experiment for reaction rate of ^{115}In(n,n')^{115m}In in Be *in situ* experiment.

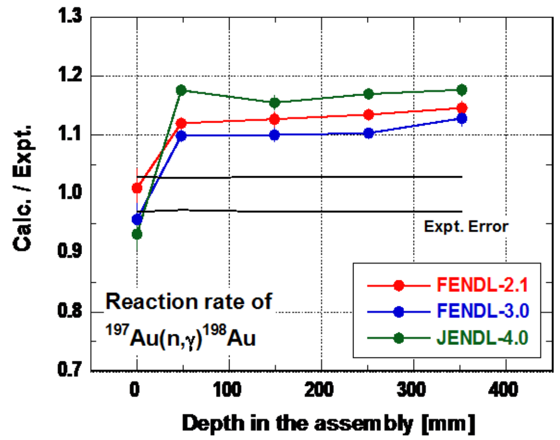

Fig. 12d: Ratios of calculation to experiment for reaction rate of ^{197}Au(n,γ)^{198}Au in Be *in situ* experiment.

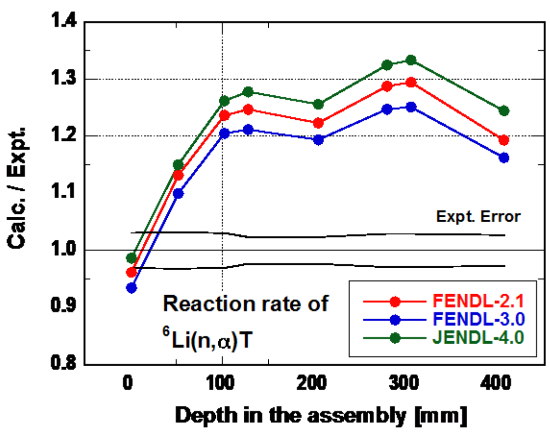

Fig. 12e: Ratios of calculation to experiment for reaction rate of ^{6}Li(n,α)^{3}T in Be *in situ* experiment.

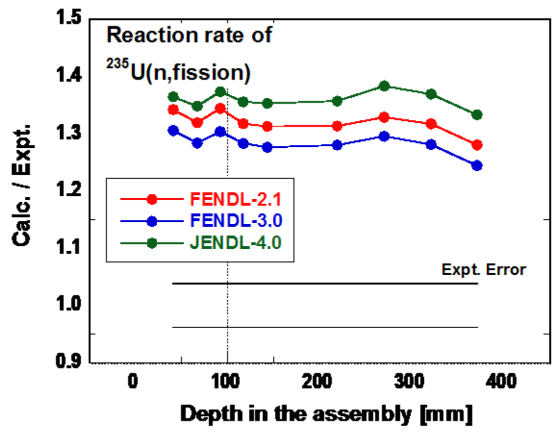

Fig. 12f: Ratios of calculation to experiment for ^{235}U fission rate in Be *in situ* experiment.

Fig. 12: Results obtained for the Be in-situ experiment at FNS showing neutron flux spectra and C/E ratios for measured reaction rates.

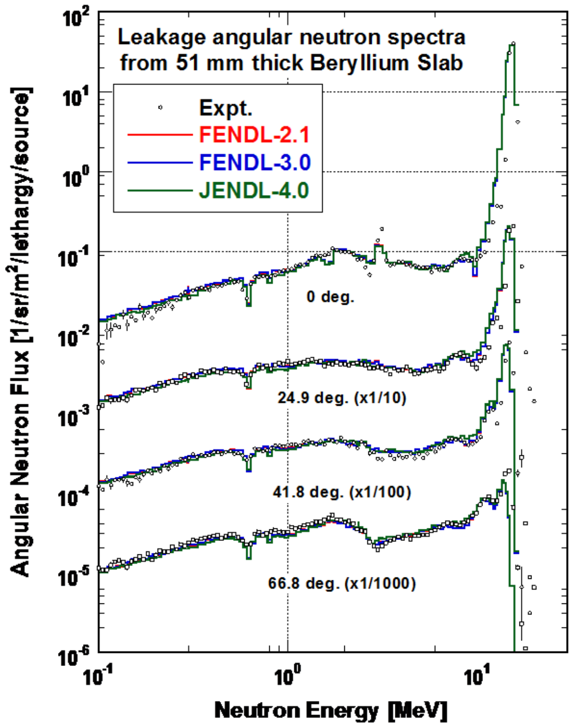	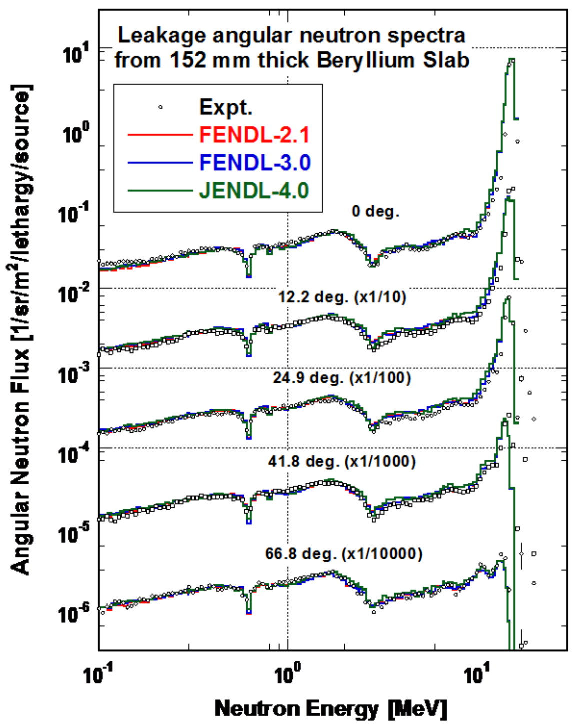
Fig. 13a: Angular neutron leakage spectra from 51 mm thick Be slab.	**Fig. 13b:** Angular neutron leakage spectra from 152 mm thick Be slab.

Fig. 13: Results obtained for the Be ToF-experiment at FNS showing angular neutron leakage spectra for 51 and 152 mm thick slabs.

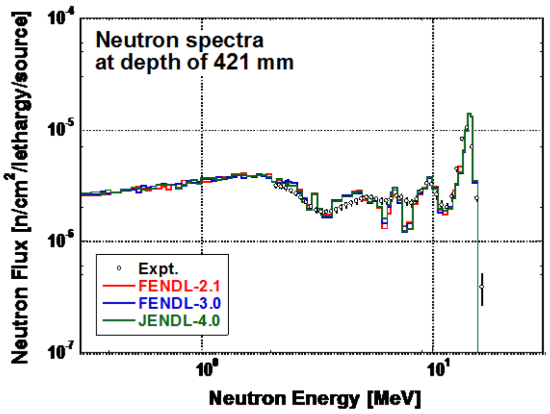

Fig. 14a: Neutron spectra at 421 mm in C *in situ* experiment

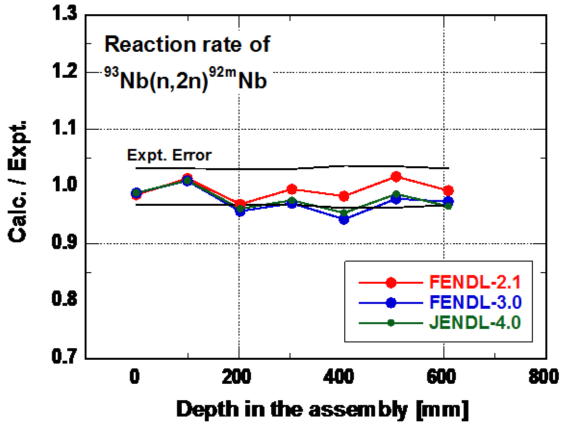

Fig. 14b: Ratios of calculation to experiment for reaction rate of ^{93}Nb(n,2n)^{92m}Nb in C *in situ* experiment.

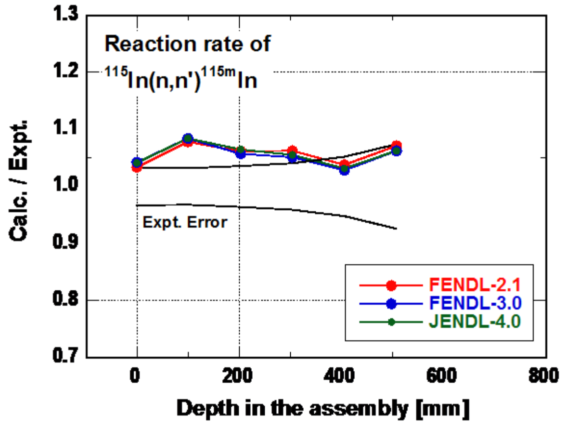

Fig. 14c: Ratios of calculation to experiment for reaction rate of ^{115}In(n,n')^{115m}In in C *in situ* experiment.

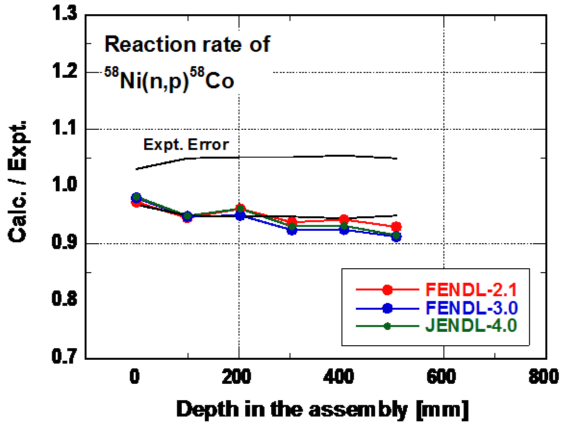

Fig. 14d: Ratios of calculation to experiment for reaction rate of ^{58}Ni(n,p)^{58}Co in C *in situ* experiment.

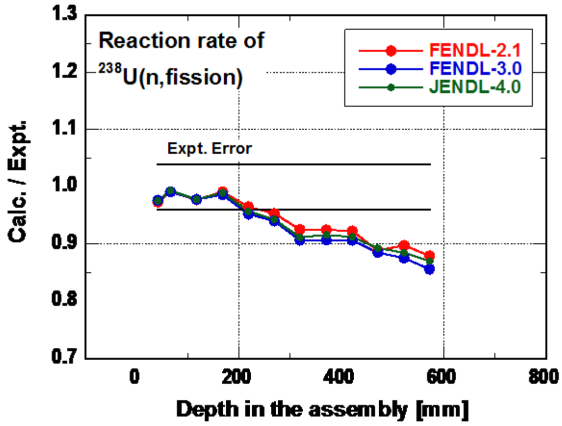

Fig. 14e: Ratios of calculation to experiment for ^{238}U fission rate in C *in situ* experiment.

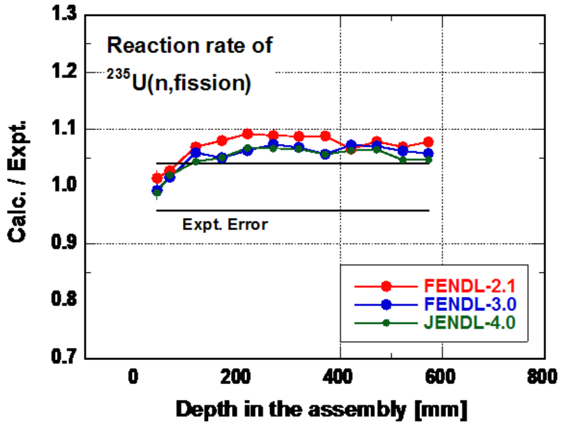

Fig. 14f: Ratios of calculation to experiment for ^{238}U fission rate in C *in situ* experiment.

Fig. 14: Results obtained for the C (graphite) in-situ experiment at FNS showing neutron flux spectra and C/E ratios for measured reaction rates.

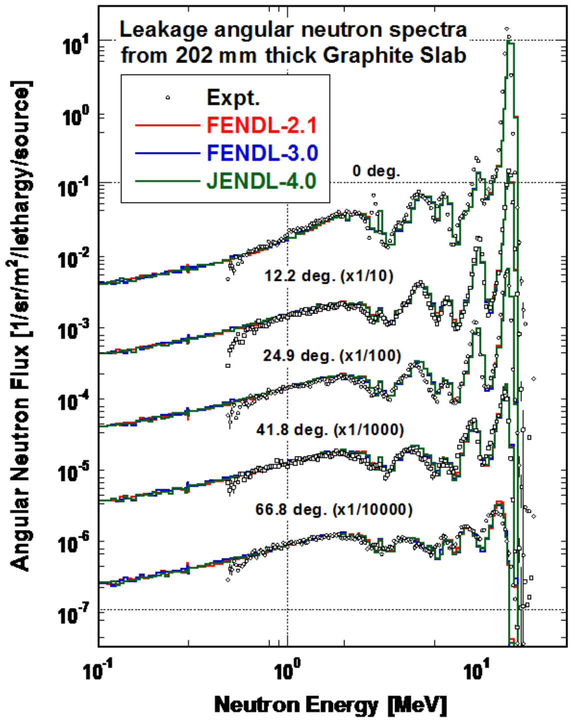	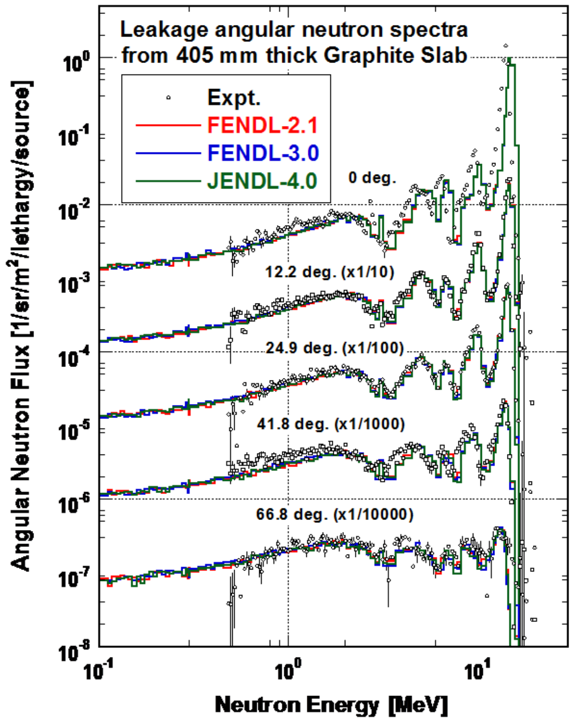
Fig. 15a: Leakage angular neutron spectra from 202 mm thick graphite slab.	**Fig. 15b:** Leakage angular neutron spectra from 405 mm thick graphite slab.

Fig. 15: Results obtained for the C (graphite) ToF-experiment at FNS showing angular neutron leakage spectra for 202 and 405 mm thick slabs.

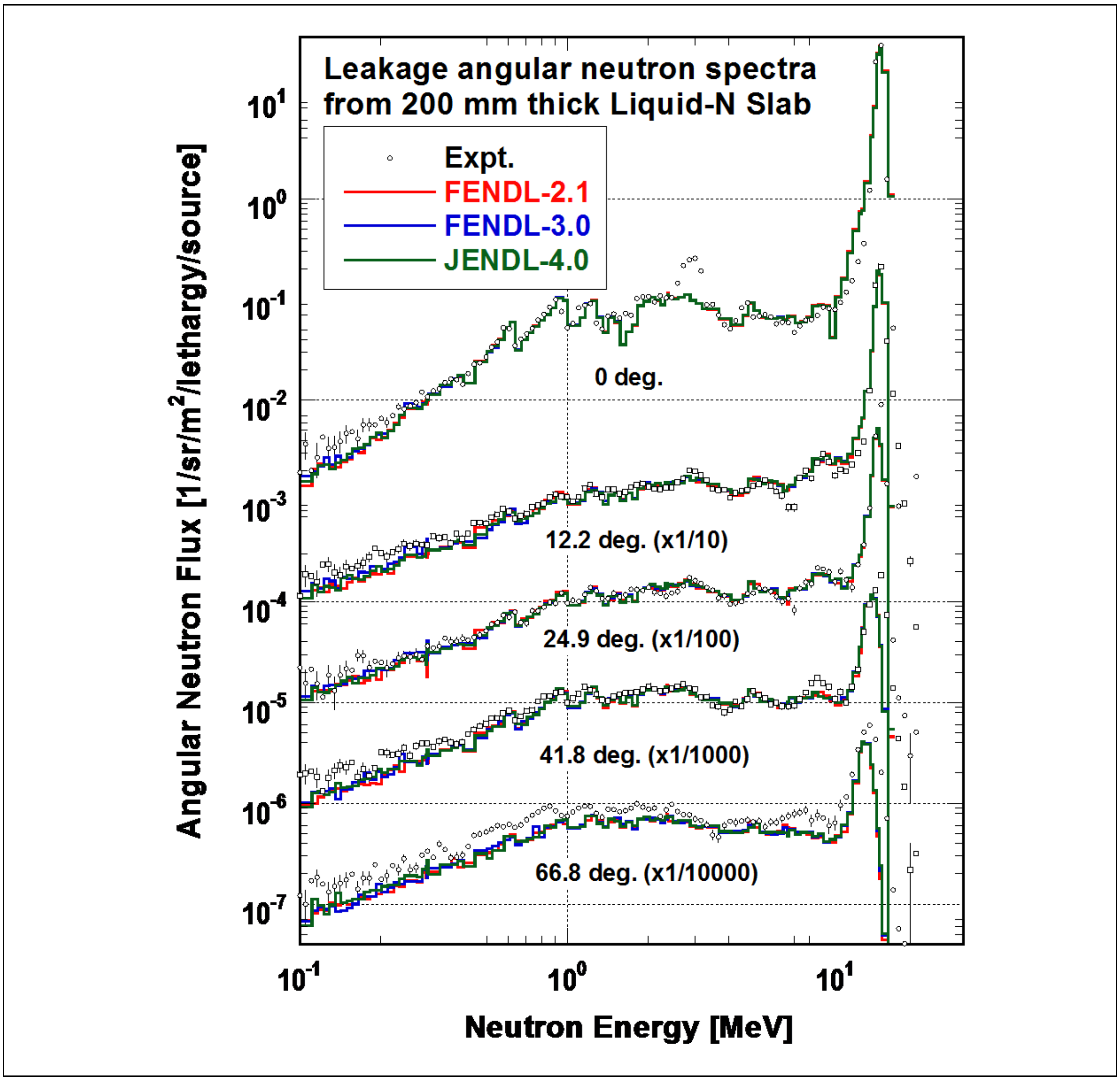

Fig. 16: Results obtained for the liquid N_2 ToF-experiment at FNS showing angular neutron leakage spectra for a 200 thick liquid nitrogen slab.

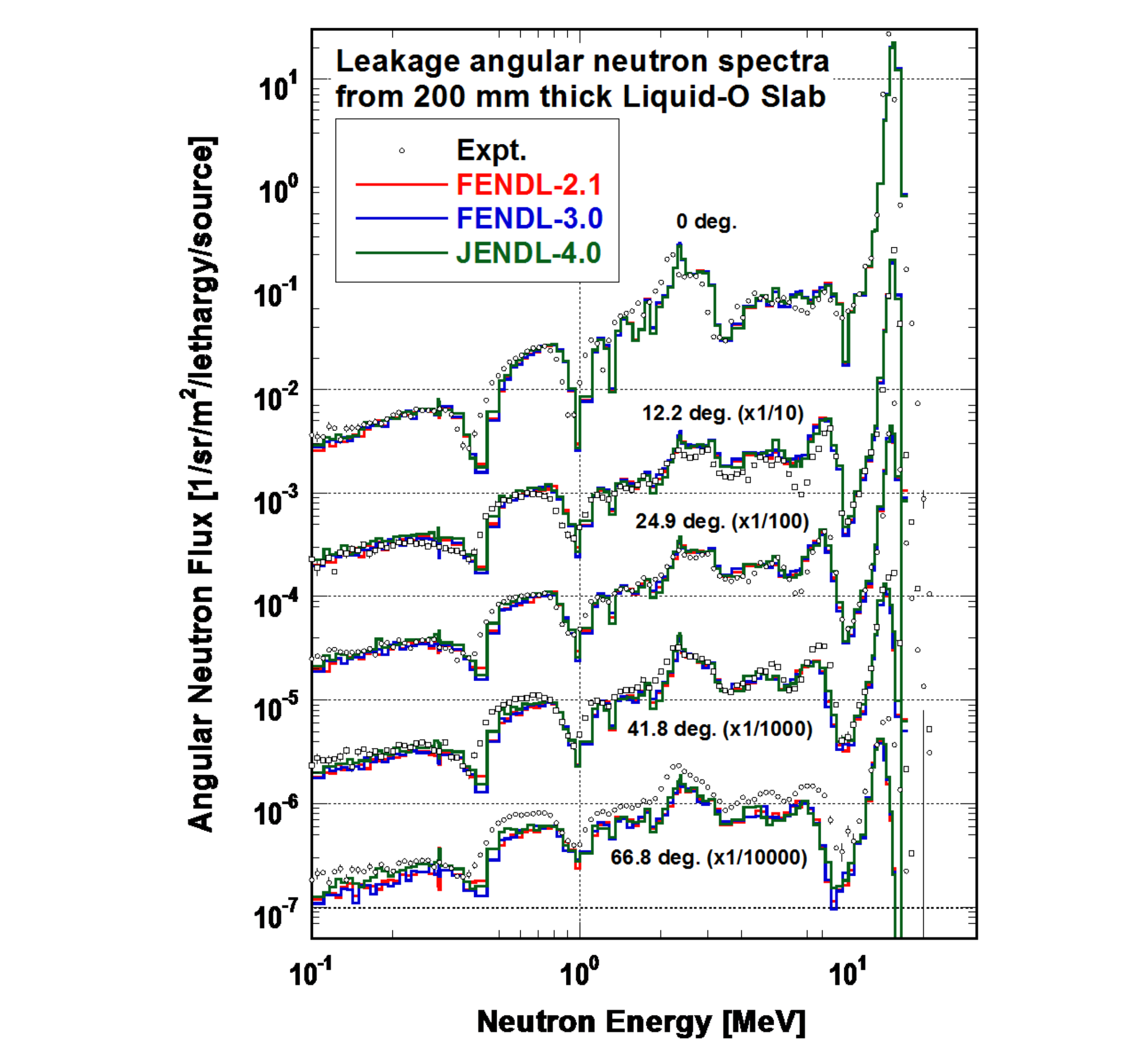

Fig. 17: Results obtained for the liquid O_2 ToF-experiment at FNS showing angular neutron leakage spectra for a 200 thick liquid oxygen slab.

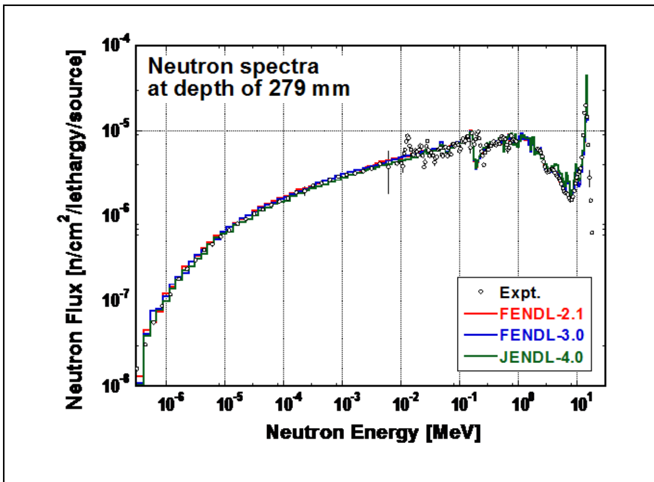

Fig. 18a: Neutron spectra at 279 mm in SiC *in situ* experiment.

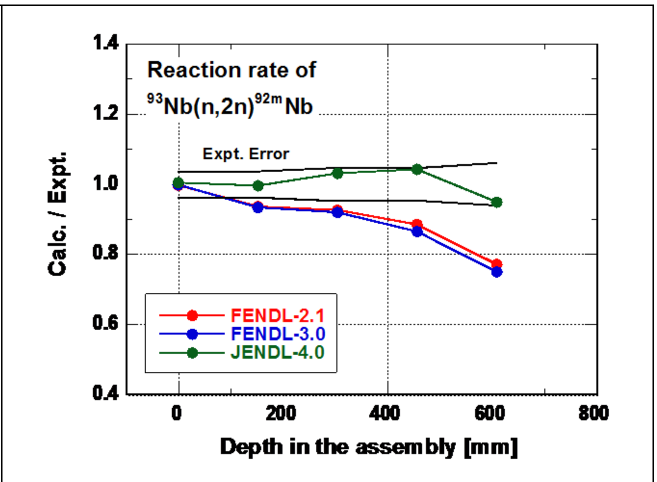

Fig. 18b: Ratios of calculation to experiment for reaction rate

of ^{93}Nb(n,2n)^{92m}Nb in SiC *in situ* experiment

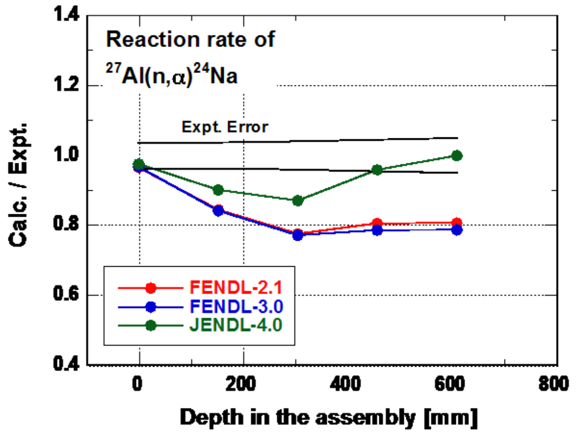

Fig. 18c: Ratios of calculation to experiment for reaction rate of ^{27}Al(n,α)^{24}Na in SiC *in situ* experiment.

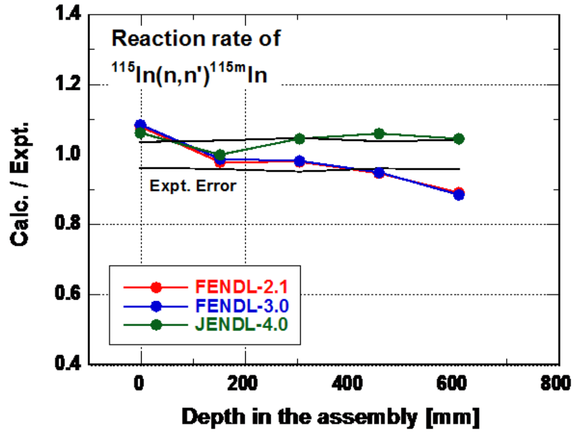

Fig. 18d: Ratios of calculation to experiment for reaction rate of ^{115}In(n,n')^{115m}In in SiC *in situ* experiment.

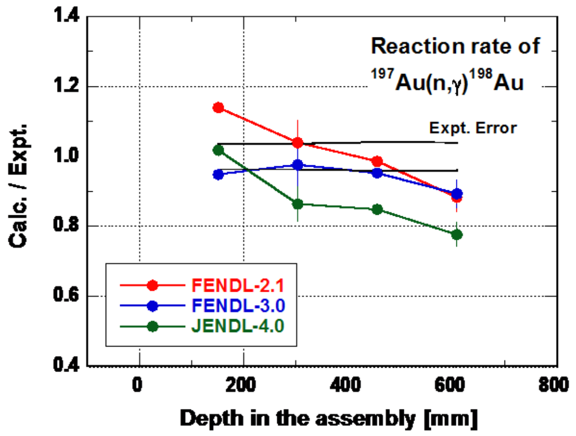

Fig. 18e: Ratios of calculation to experiment for reaction rate of ^{197}Au(n,γ)^{198}Au in SiC *in situ* experiment.

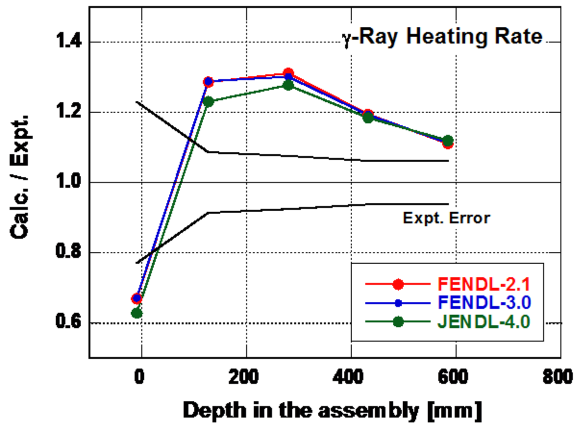

Fig. 18f: Ratios of calculation to experiment for gamma heating rate in SiC *in situ* experiment.

Fig. 18: Results obtained for the SiC in-situ experiment at FNS showing neutron flux spectra and C/E ratios for measured reaction rates.

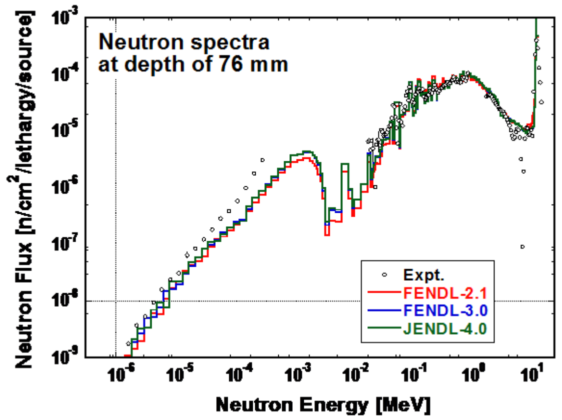

Fig. 19a: Neutron spectra at 76 mm in V *in situ* experiment.

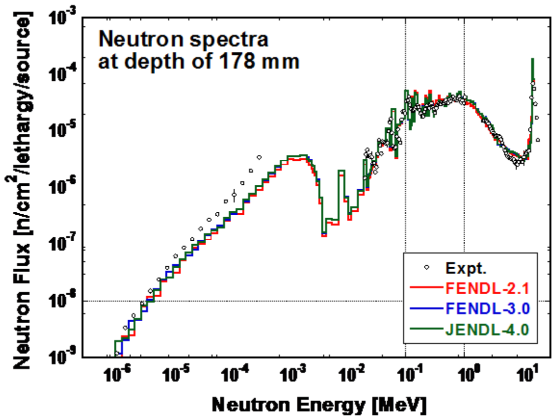

Fig. 19b: Neutron spectra at 178 mm in V *in situ* experiment.

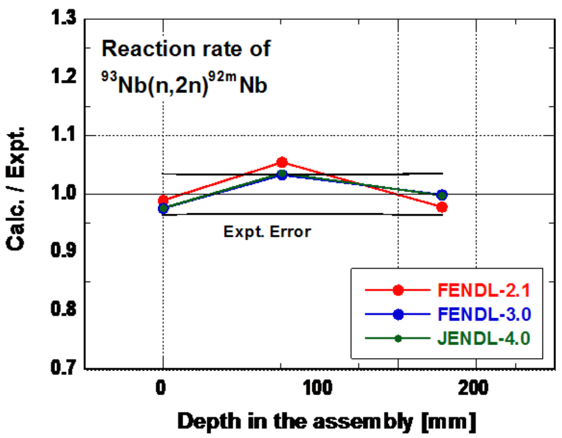

Fig. 19c: Ratios of calculation to experiment for reaction rate of ^{93}Nb(n,2n)^{92m}Nb in V *in situ* experiment.

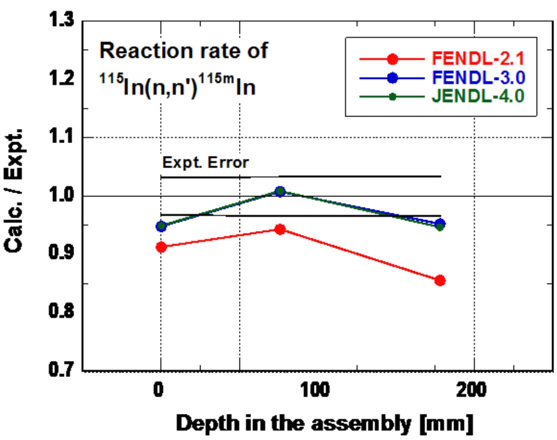

Fig. 19d: Ratios of calculation to experiment for reaction rate of ^{115}In(n,n')^{115m}In in V *in situ* experiment.

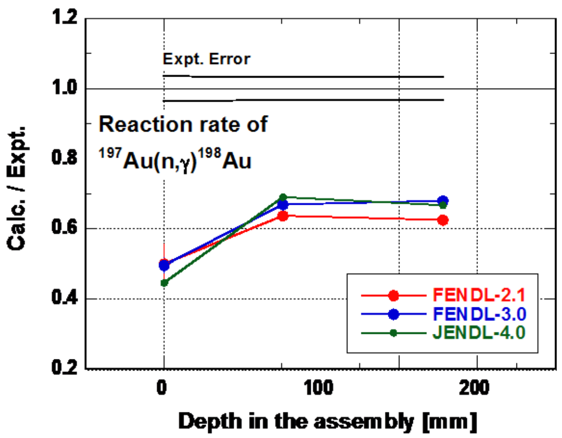

Fig. 19e: Ratios of calculation to experiment for reaction rate of ^{197}Au(n,γ)^{198}Au in V *in situ* experiment.

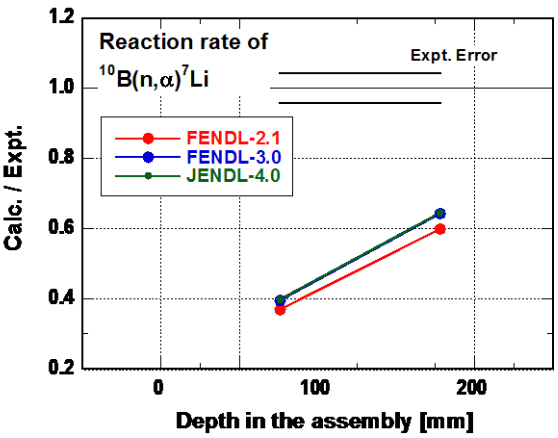

Fig. 19f: Ratios of calculation to experiment for reaction rate of ^{10}B(n,α)^{7}Li in V *in situ* experiment.

Fig. 19: Results obtained for the V in-situ experiment at FNS showing neutron flux spectra and C/E ratios for measured reaction rates.

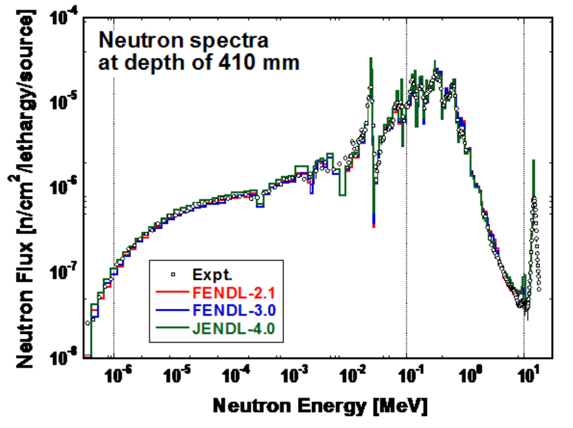

Fig. 20a: Neutron spectra at 410 mm in Fe *in situ* experiment.

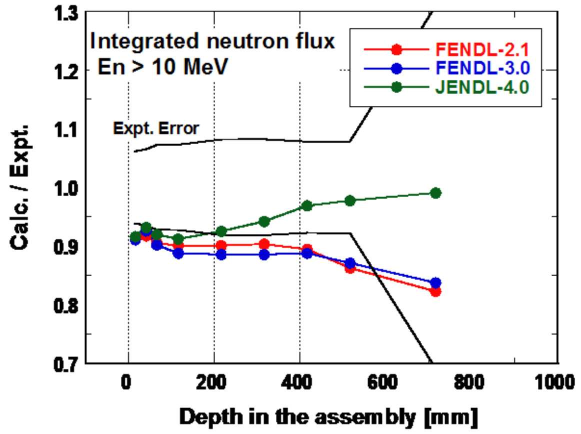

Fig. 20b: Ratios of calculation to experiment for reaction rate of neutron flux above 10 MeV in Fe *in situ* experiment.

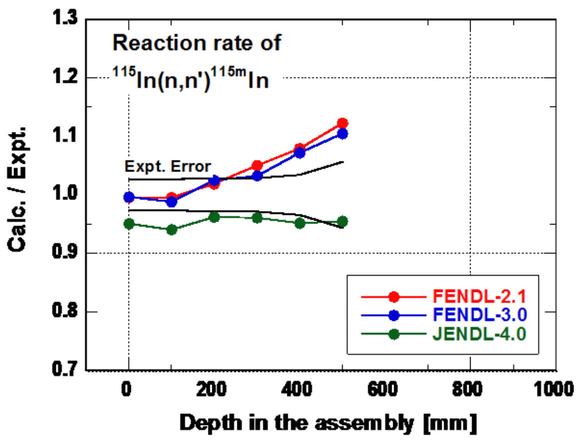

Fig. 20c: Ratios of calculation to experiment for reaction rate of ^{115}In(n,n')^{115m}In in Fe *in situ* experiment.

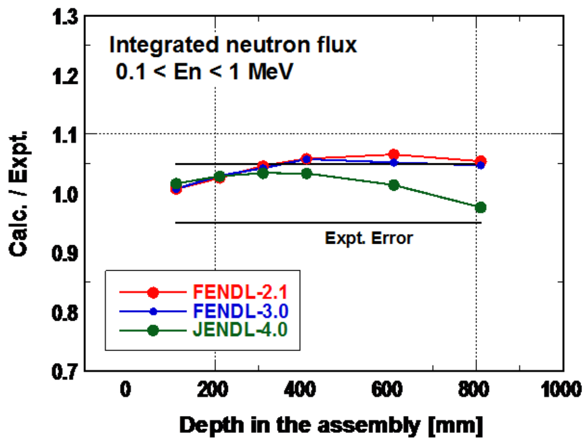

Fig. 20d: Ratios of calculation to experiment for neutron flux from 0.1 MeV to 1 MeV in Fe *in situ* experiment.

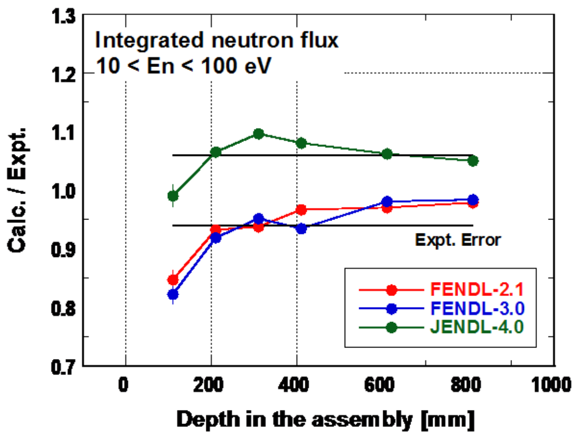

Fig. 20e: Ratios of calculation to experiment for neutron flux from 10 eV to 100 eV in Fe *in situ* experiment.

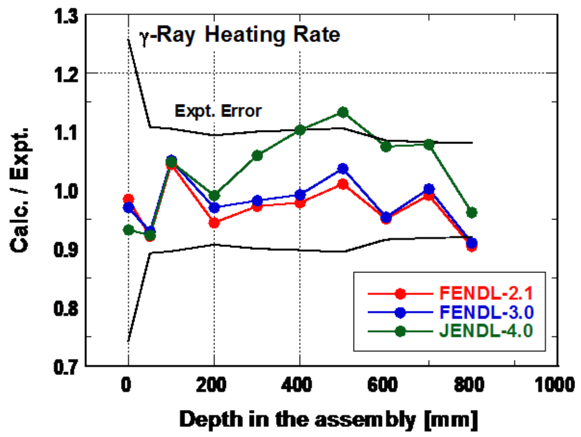

Fig. 20f: Ratios of calculation to experiment for gamma heating rate in Fe *in situ* experiment.

Fig. 20: Results obtained for the Fe in-situ experiment at FNS showing neutron flux spectra and C/E ratios for measured reaction rates.

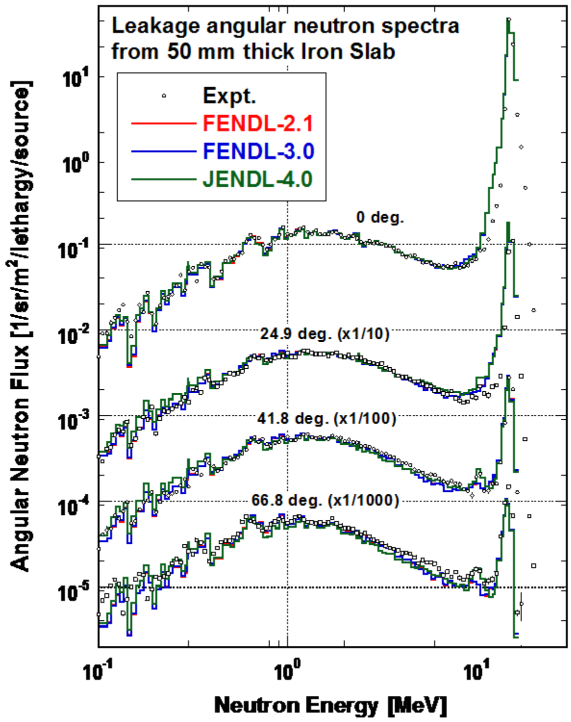

Fig. 21a: Angular neutron leakage spectra for the 50 mm thick Fe slab.

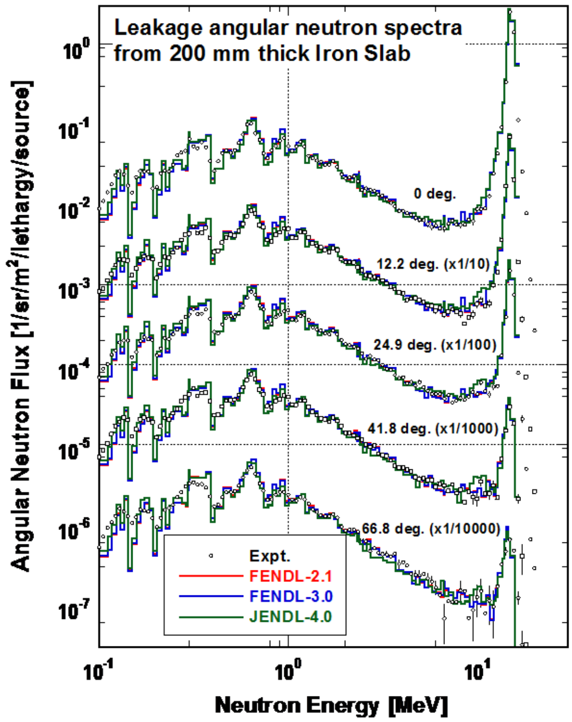

Fig. 21b: Angular neutron leakage spectra for the 200 mm thick Fe slab.

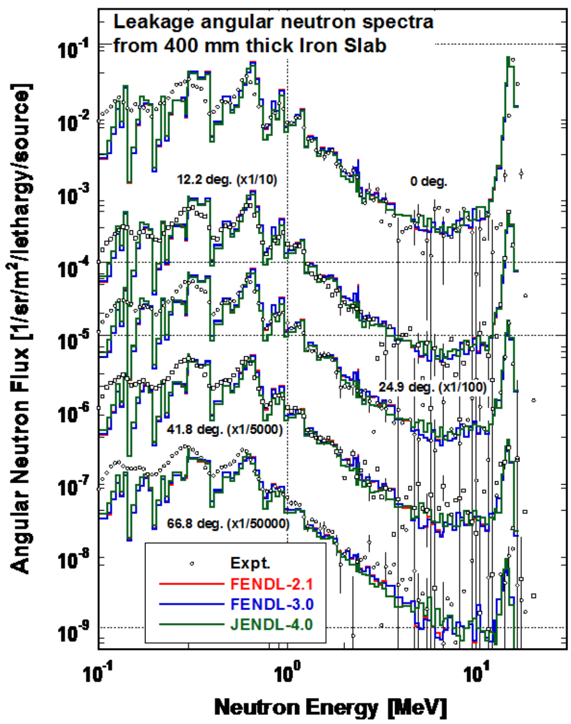

Fig. 21c: Angular neutron leakage spectra for the 400 mm thick Fe slab.

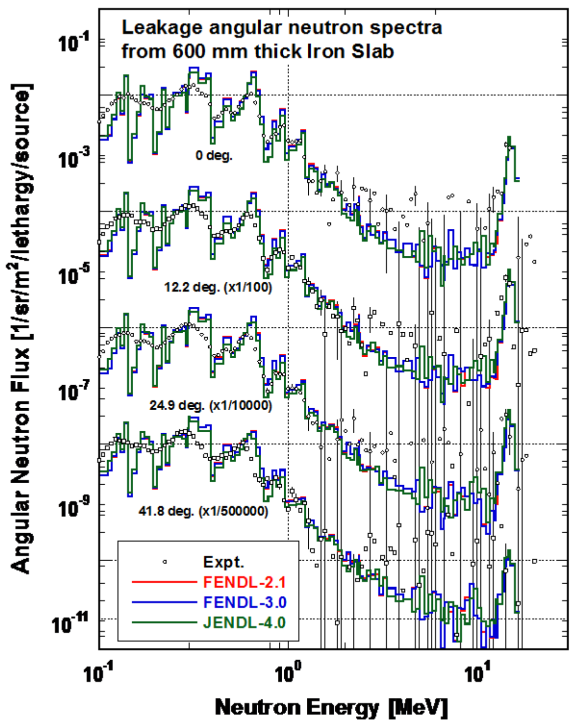

Fig. 21d: Angular neutron leakage spectra for the 600 mm thick Fe slab.

Fig. 21: Results obtained for the Fe ToF-experiment at FNS showing angular neutron leakage spectra for 50, 200, 400 and 600 mm thick slabs.

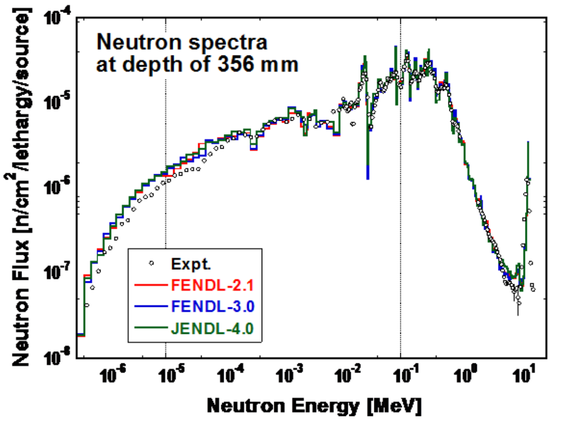

Fig. 22a: Neutron spectra at 356 mm in the SS316 *in situ* experiment.

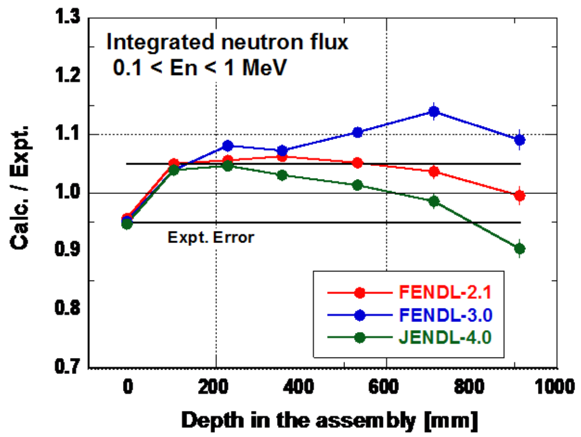

Fig. 22b: Ratios of calculation to experiment for neutron flux from 100 keV to 1 MeV in the SS316 *in situ* experiment.

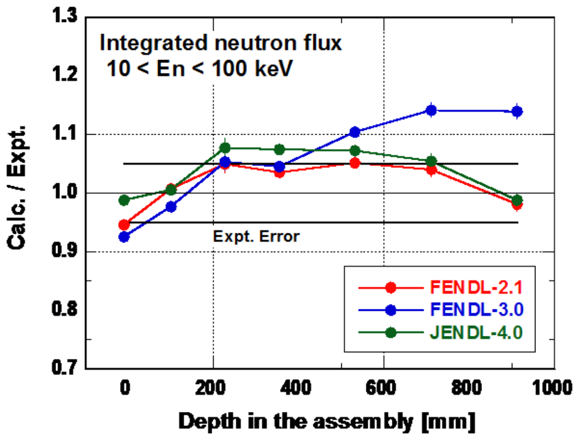

Fig. 22c: Ratios of calculation to experiment for neutron flux from 10 keV to 100 keV in the SS316 *in situ* experiment.

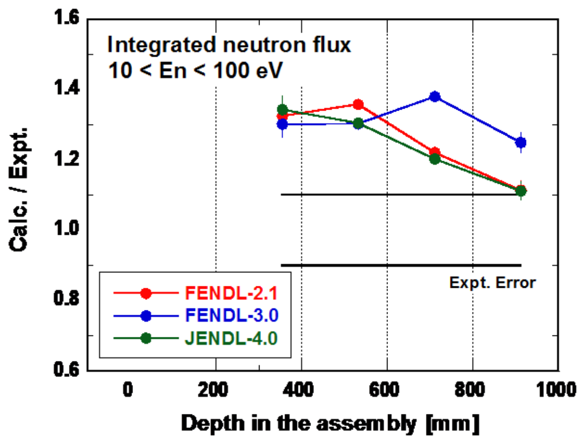

Fig. 22d: Ratios of calculation to experiment for neutron flux from 10 eV to 100 eV in the SS316 *in situ* experiment.

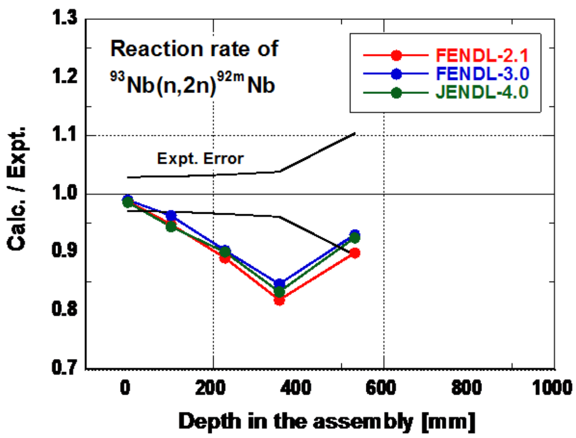

Fig. 22e: Ratios of calculation to experiment for reaction rate of ^{93}Nb(n,2n)^{92m}Nb in the SS316 *in situ* experiment.

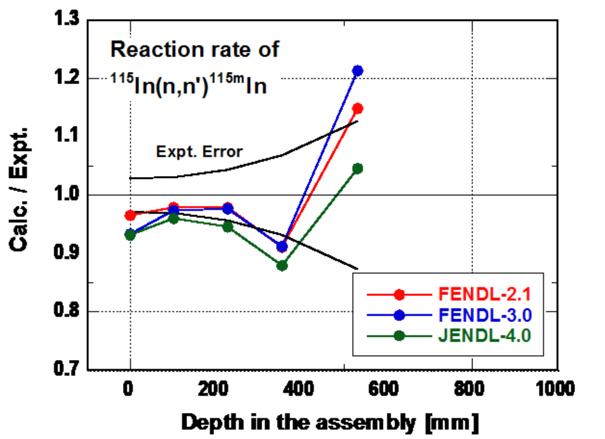

Fig. 22f: Ratios of calculation to experiment for reaction rate of ^{115}In(n,n')^{115m}In in the SS316 *in situ* experiment.

Fig. 22: Results obtained for the SS-316 in-situ experiment at FNS showing neutron flux spectra and C/E ratios for measured reaction rates.

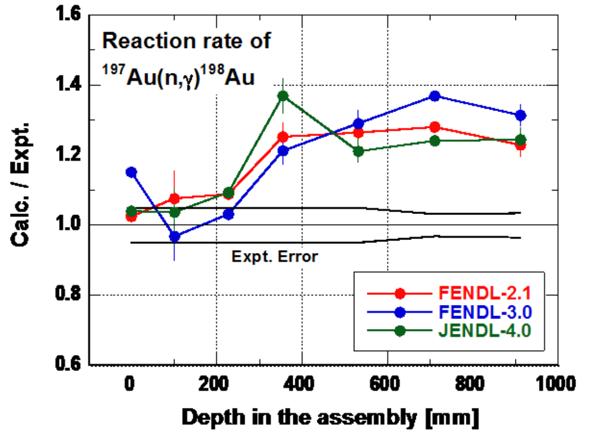

Fig. 22g: Ratios of calculation to experiment for reaction rate of $^{197}Au(n,\gamma)^{198}Au$ in the SS316 *in situ* experiment.

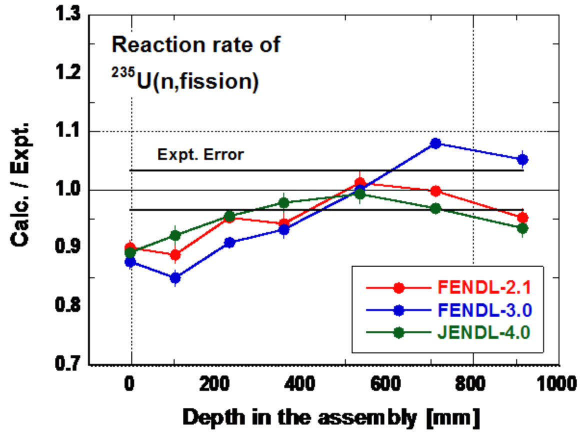

Fig. 22h: Ratios of calculation to experiment for ^{235}U fission rate in the SS316 *in situ* experiment.

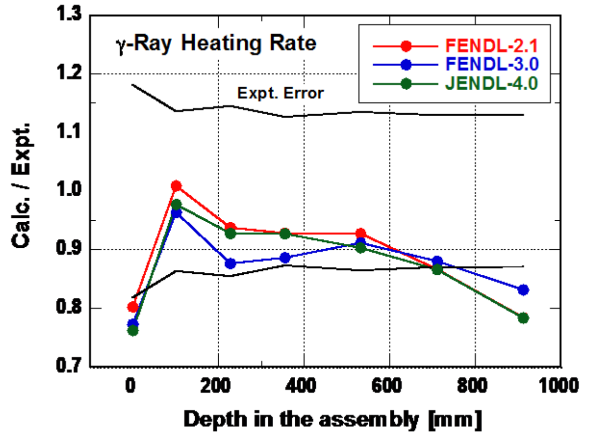

Fig. 22i: Ratios of calculation to experiment for gamma heating rate in the SS316 *in situ* experiment.

Fig. 22 (cont'd): Results obtained for the SS-316 in-situ experiment at FNS showing C/E ratios for measured reaction rates.

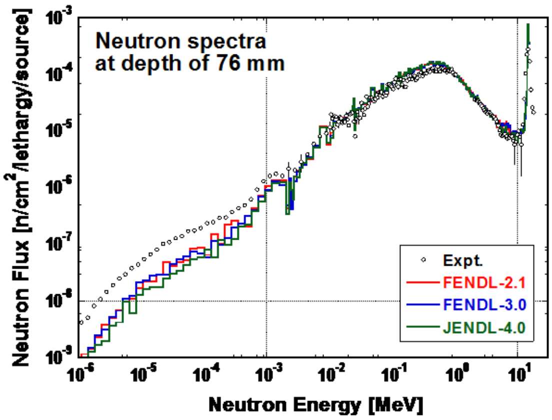

Fig. 23a: Neutron spectra at 76 mm in the Cu *in situ* experiment.

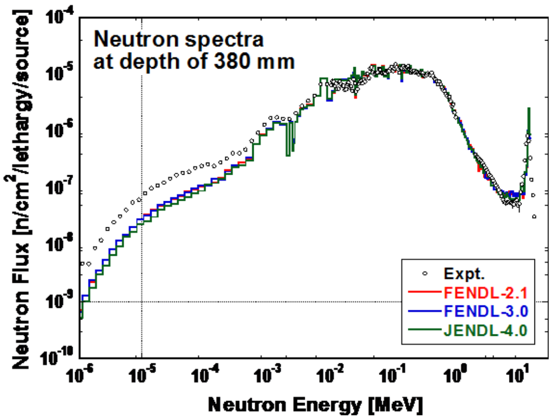

Fig. 23b: Neutron spectra at 380 mm in the Cu *in situ* experiment.

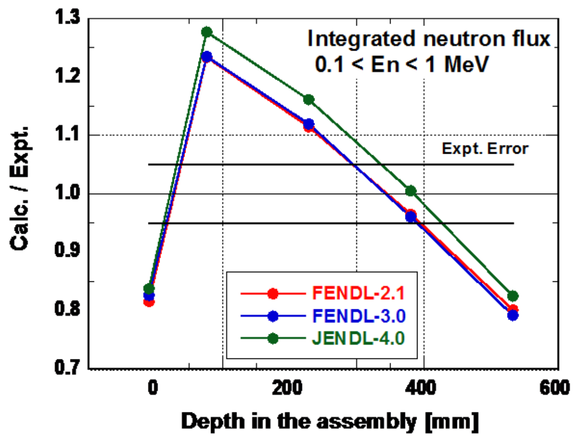

Fig. 23c: Ratios of calculation to experiment for neutron flux from 100 keV to 1 MeV in the Cu *in situ* experiment.

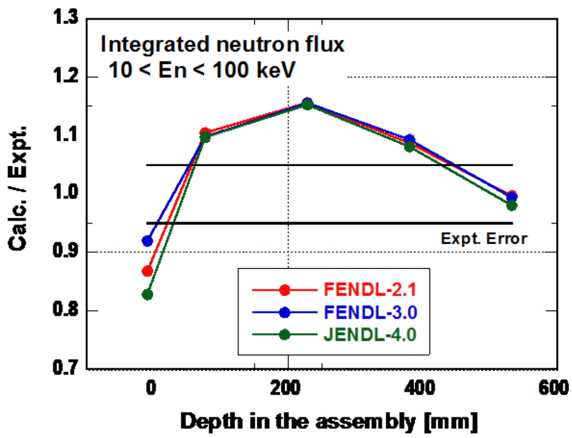

Fig. 23d: Ratios of calculation to experiment for neutron flux from 10 keV to 100 keV in the Cu *in situ* experiment.

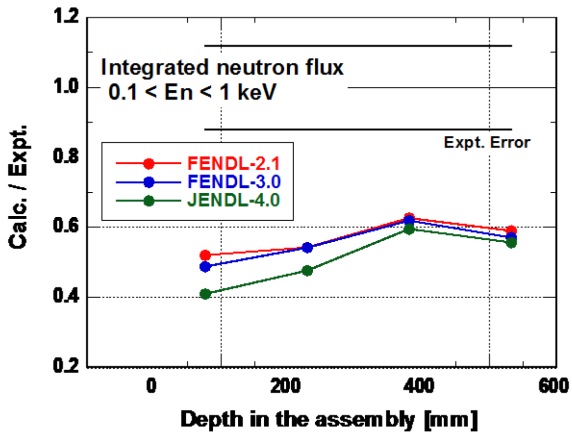

Fig. 23e: Ratios of calculation to experiment for neutron flux from 0.1 keV to 1 keV in the Cu *in situ* experiment.

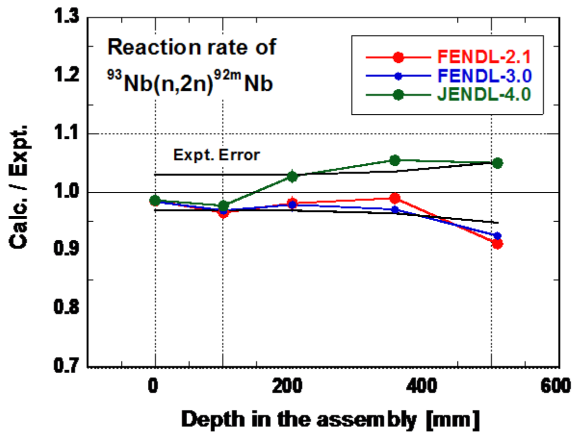

Fig. 23f: Ratios of calculation to experiment for reaction rate of ^{93}Nb(n,2n)^{92m}Nb in the Cu *in situ* experiment.

Fig. 23: Results obtained for the Cu in-situ experiment at FNS showing neutron flux spectra and C/E ratios for measured reaction rates.

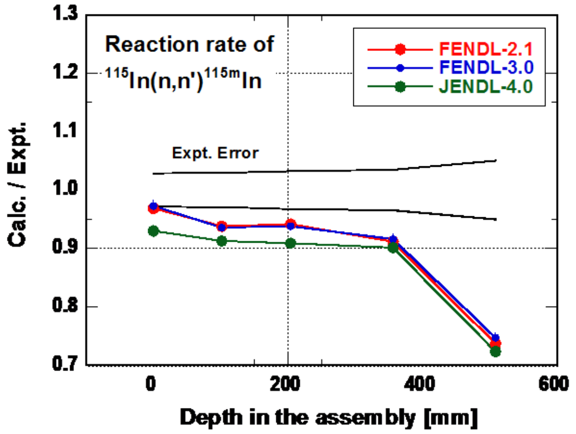	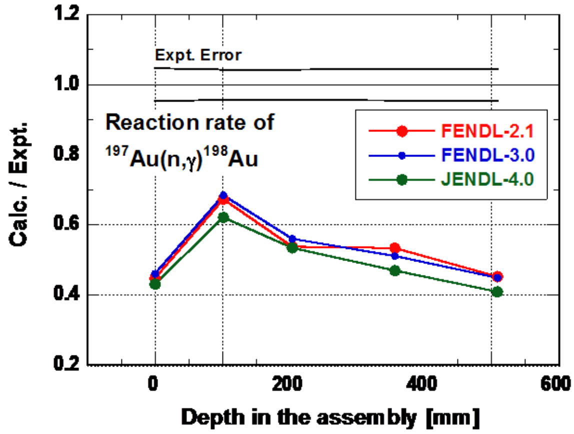
Fig. 23g: Ratios of calculation to experiment for reaction rate of ^{115}In(n,n')^{115m}In in the Cu *in situ* experiment.	**Fig. 23h:** Ratios of calculation to experiment for reaction rate of ^{197}Au(n,γ)^{198}Au in the Cu *in situ* experiment.

Fig. 23 (cont'd): Results obtained for the Cu in-situ experiment at FNS showing C/E ratios for measured reaction rates.

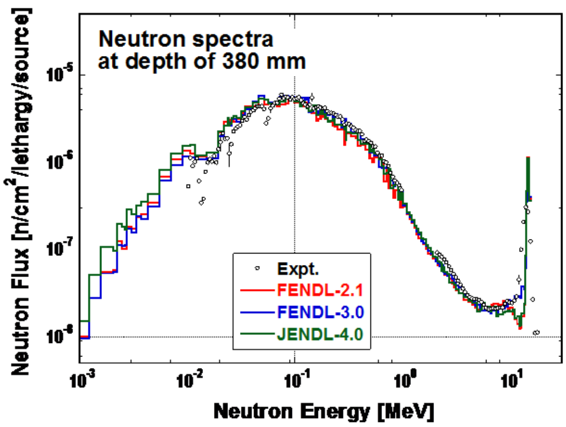

Fig. 24a: Neutron spectra at 380 mm in the W *in situ* experiment.

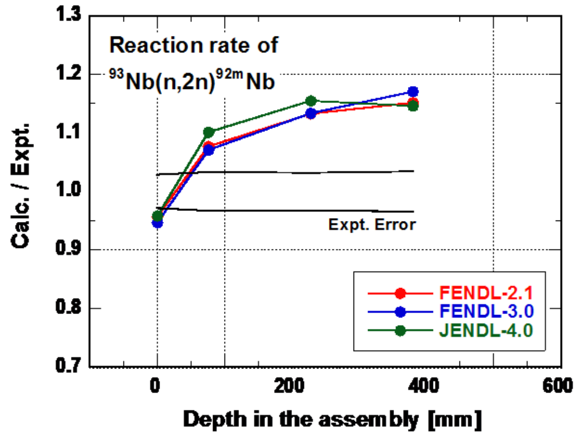

Fig. 24b: Ratios of calculation to experiment for reaction rate of ^{93}Nb(n,2n)^{92m}Nb in the W *in situ* experiment.

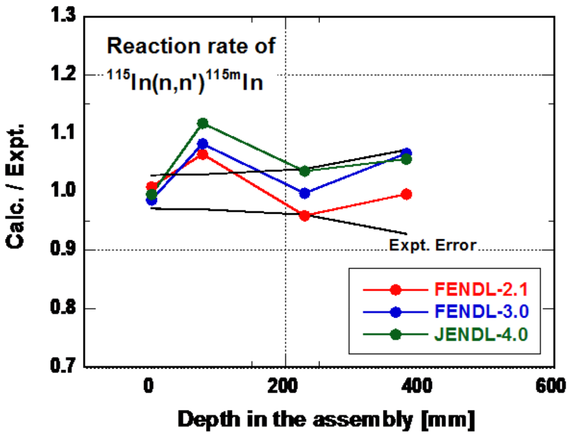

Fig. 24c: Ratios of calculation to experiment for reaction rate of ^{115}In(n,n')^{115m}In in the W *in situ* experiment

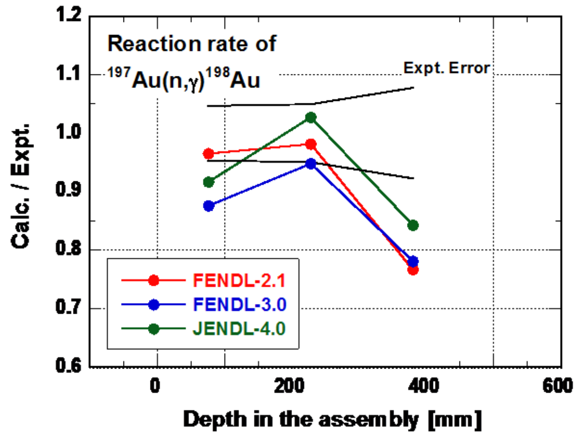

Fig. 24d: Ratios of calculation to experiment for reaction rate of ^{197}Au(n,γ)^{198}Au in the W *in situ* experiment.

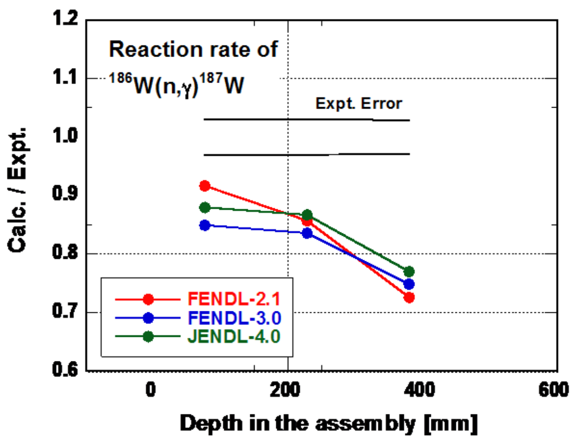

Fig. 24e: Ratios of calculation to experiment for reaction rate of ^{186}W(n,γ)^{187}W in the W *in situ* experiment.

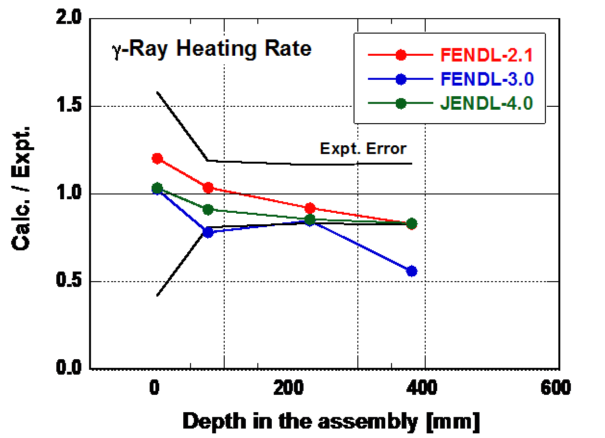

Fig. 24f: Ratios of calculation to experiment for gamma heating rate in the W *in situ* experiment.

Fig. 24: Results obtained for the W in-situ experiment at FNS showing neutron flux spectra and C/E ratios for measured reaction rates.

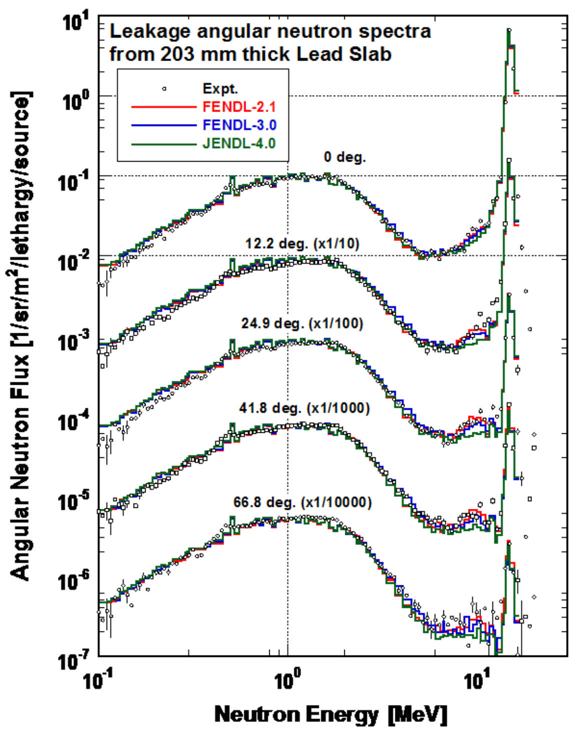

Fig. 25a: Angular neutron leakage spectra for 203 mm thick Pb slab.

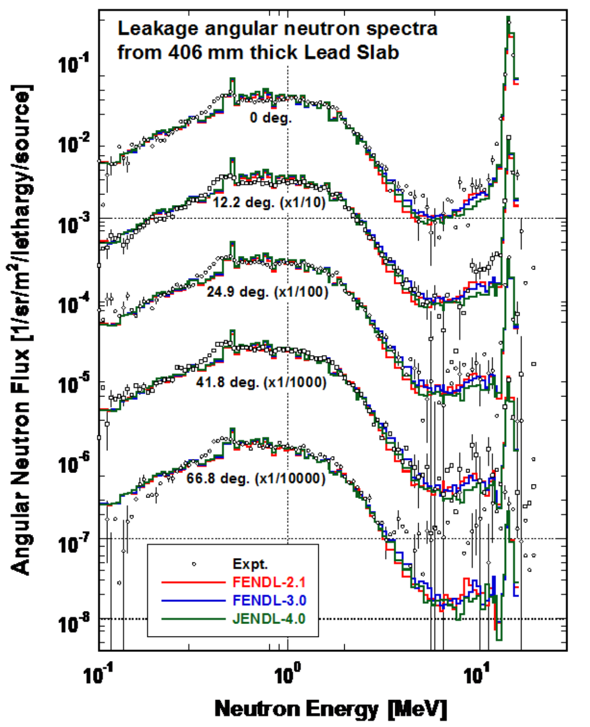

Fig. 25b: Angular neutron leakage spectra for 406 mm thick Pb slab.

Fig. 25: Results obtained for the Pb ToF-experiment at FNS showing angular neutron leakage spectra for 203 and 406 mm thick slabs.

4.2 FNG experiments

The benchmark experiments performed previously at FNG, ENEA Frascati, which were used for the benchmarking of the FENDL-3 data in this report, comprise the ITER bulk shield mock-up experiment, the tungsten neutron transmission experiment and the tritium breeding validation experiments on mock-ups of the HCPB and HCLL Test Blanket modules.

ITER bulk shield mock-up experiment

The ITER bulk shield mock-up experiment was performed to validate the shielding performance of the ITER inboard blanket/shield system [13]. The mock-up consisted of a 94 cm thick shielding block made of alternate plates of SS-316 and Perspex backed by a 30 cm thick block of alternating SS-316 and copper plates to simulate the toroidal field (TF) coils. Neutron and photon flux spectra were measured at the two positions A (41.4 cm) and B (87.6 cm) in the mock-up in the energy range between 20 keV and 15 MeV. Position A corresponds to the back plate of the shielding blanket in ITER while position B is located at the back of the vacuum vessel near the TF-coil mock-up.

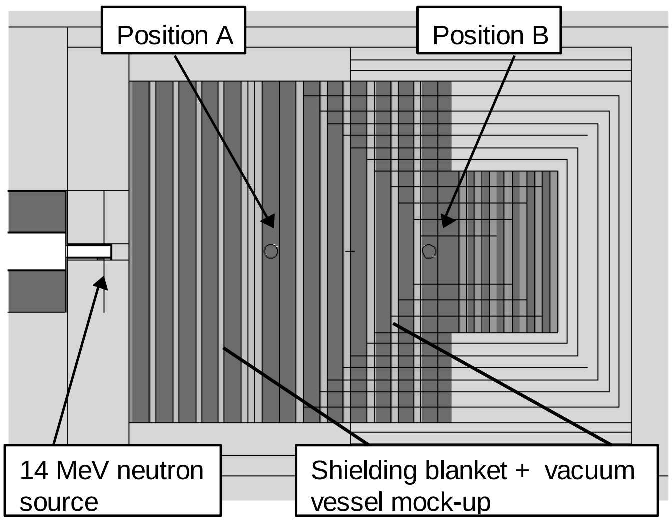

Fig. 26: Schematic set-up of the ITER bulk shield experiment at FNG with measurement positions indicated.

Fig. 27 shows the comparison of the measured and calculated neutron spectra. FENDL-3.0 well reproduces the experimental data and there is no significant difference between the results obtained with FENDL-2.1. When comparing C/E (calculation/experiment) ratios for the neutron flux above 0.1 MeV, FENDL-3.0 gives 0.90 and 0.75 for the front and the rear position, respectively, while FENDL-2.1 gives 0.89 and 0.74. Table X summarizes the C/E ratios for the neutron flux integrated from 10 to 16 MeV which corresponds to the neutron source peak. At the deep position B one can see a noticeable difference between FENDL-3/SLIB4 and FENDL-2.1 showing a better result for the FENDL-3 data.

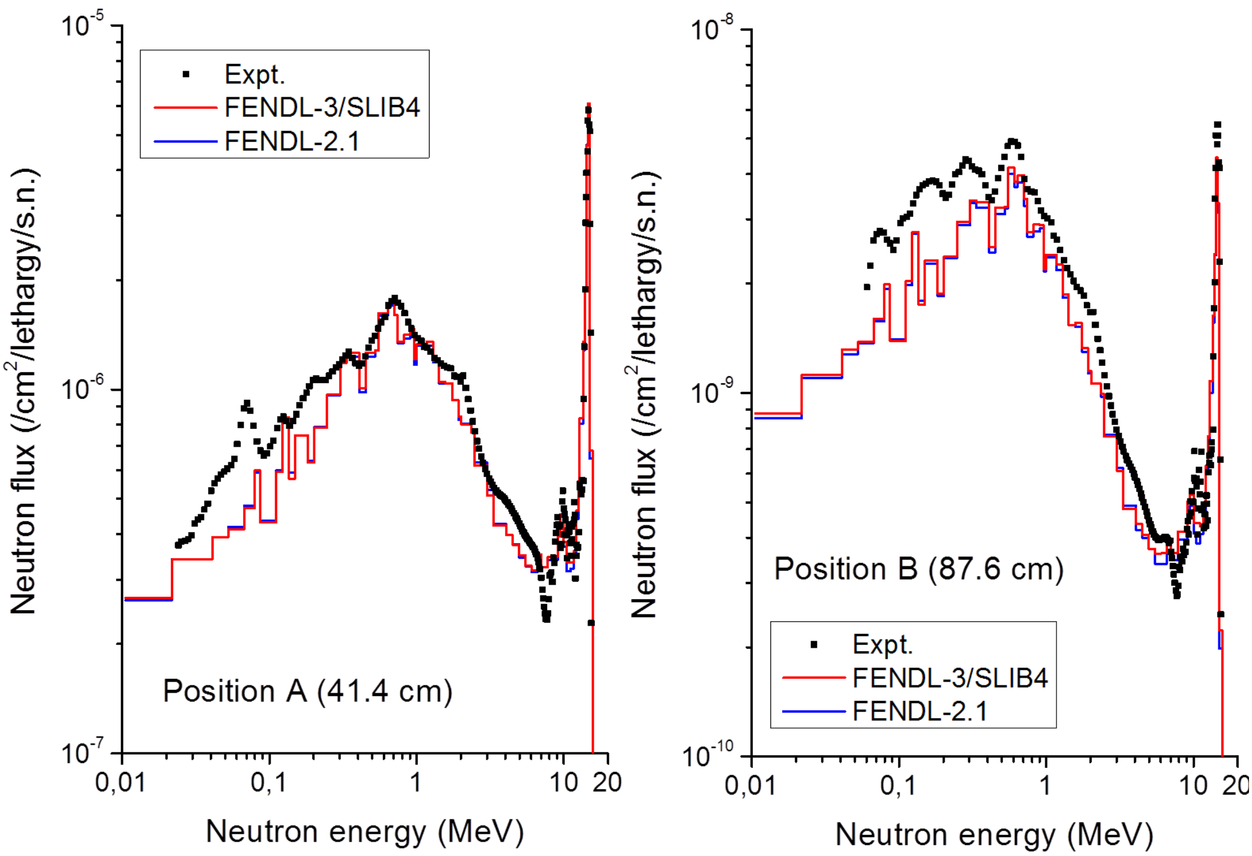

Fig. 27: Results obtained for the neutron flux spectra in the front (41.4 cm) and rear (87.6 cm) positions of the ITER shield mock-up experiment at FNG.

TABLE X: CALCULATION-TO-EXPERIMENT (C/E) RATIOS FOR THE NEUTRON FLUX INTEGRATED FROM 10 TO 16 MeV AS OBTAINED FOR THE ITER BULK SHIELD EXPERIMENT AT FNG.

Nuclear data library	Position A	Position B
FENDL-3/SLIB4	1.07	1.00
FENDL-2.1	1.06	0.96
JEFF-3.1.1	1.08	0.99
ENDF/B-VII.0	1.09	0.93
JENDL-4.0	1.08	0.99

Fig. 28 shows the comparison of the measured and calculated photon spectra. Again FENDL-3.0 reproduces well the experimental data and gives slightly larger results than FENDL-2.1. The C/E ratios for the integrated photon flux, calculated with FENDL-3.0, amount to 1.02 and 0.96 for the front and the rear position, respectively, and 0.98 and 0.89, respectively, calculated with FENDL-2.1, see Table XI. Thus FENDL-3 shows an improvement over FENDL-2.1 for the photon flux at the deep position B in the mock-up. This is a significant result which affects the nuclear heating and photon radiation loads to the super-conducting magnet in ITER.

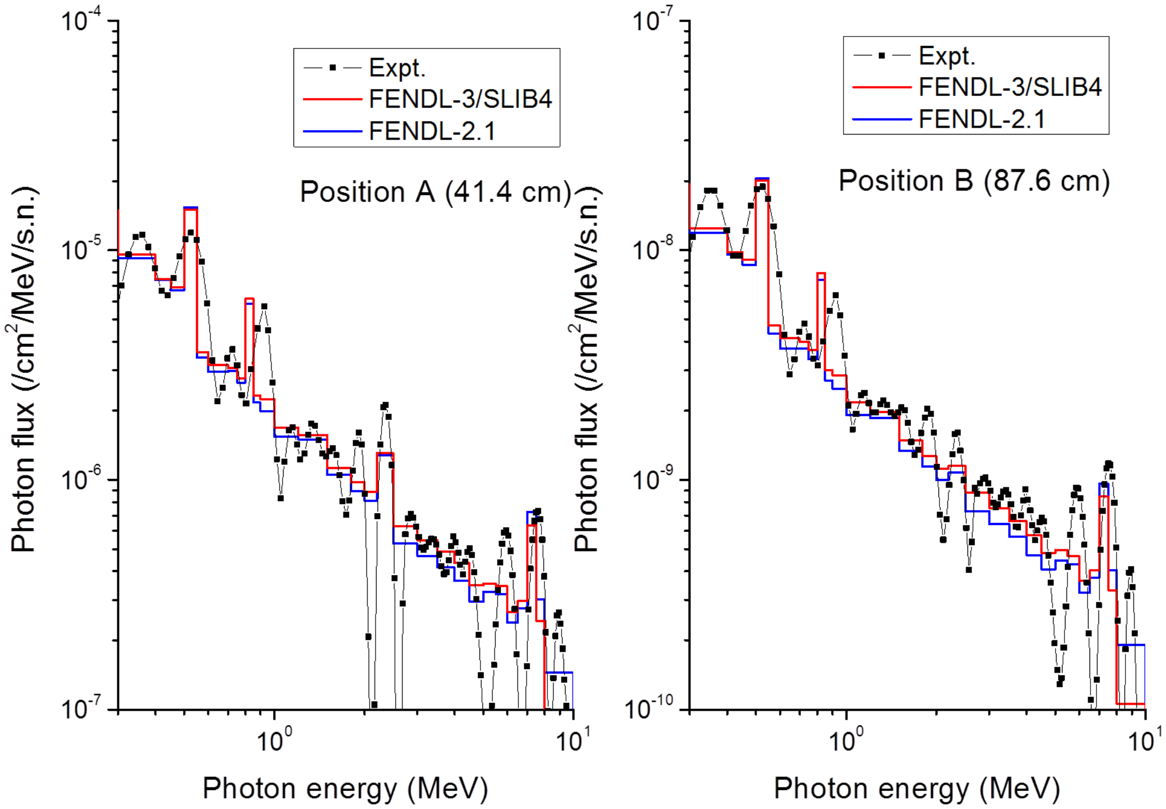

Fig. 28: Results obtained for the photon flux spectra in the front (41.4 cm) and rear (87.6 cm) positions of the ITER shield mock-up experiment at FNG.

TABLE XI: CALCULATION-TO-EXPERIMENT (C/E) RATIOS FOR THE PHOTON FLUX INTEGRATED FROM 0.4 TO 10 MEV AS OBTAINED FOR THE ITER BULK SHIELD EXPERIMENT AT FNG.

Nuclear data	Position A	Position B
FENDL-3/SLIB4	1.02	0.96
FENDL-2.1	1.00	0.93
JEFF-3.1.1	0.97	0.93
ENDF/B-VII.0	0.97	0.90
JENDL-4.0	1.02	0.97

W neutron transmission experiment

The tungsten benchmark experiment [14] was conducted at FNG in order to check and validate the neutron cross sections of tungsten which is a candidate material for high flux components in fusion reactors. The dimensions of the rectangular W assembly amount to 47 cm (width) × 47 cm (height) × 49 cm (depth). Neutron and photon flux spectra were measured with an NE-213 scintillation spectrometer at four positions (P1–P4, 5, 15, 20 and 35 cm) inside the W block, see Fig. 29.

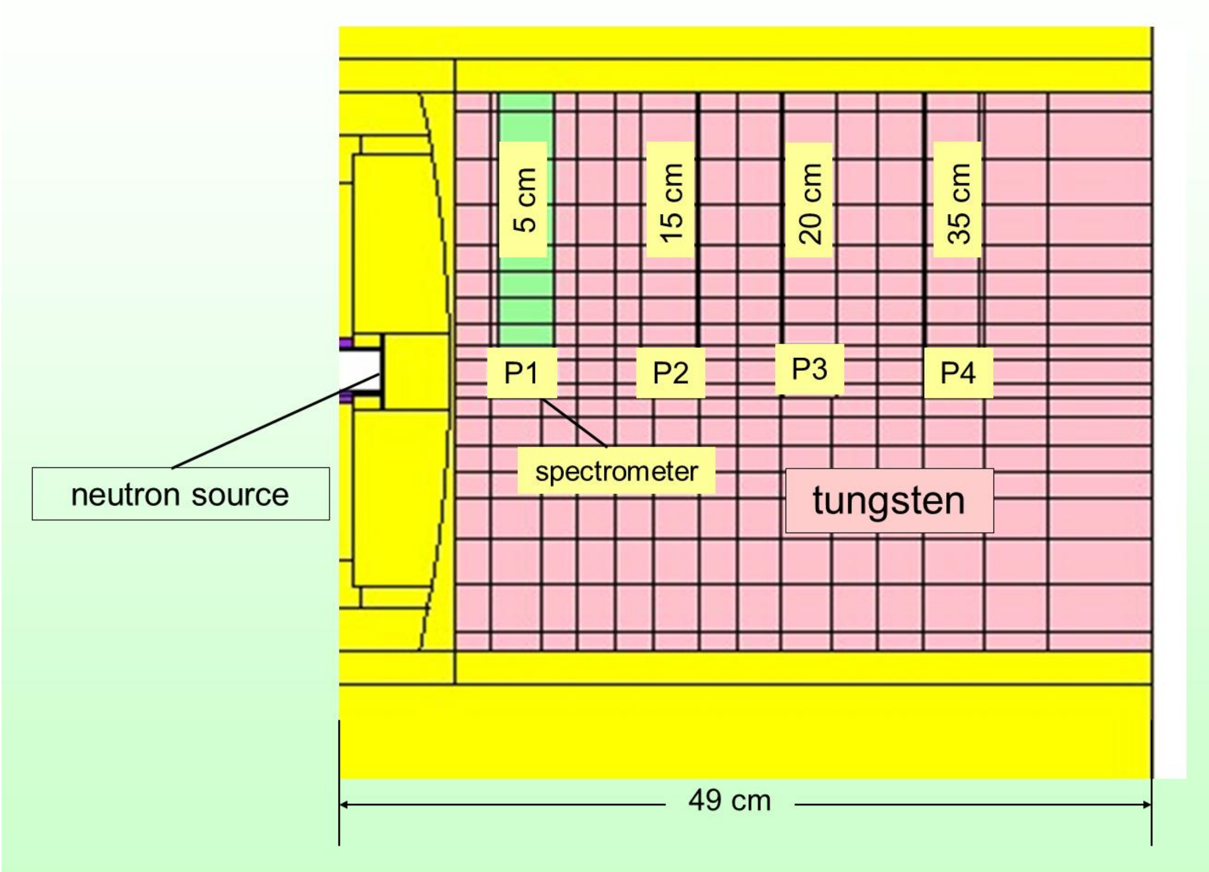

Fig. 29: Schematic set-up of the W benchmark experiment at FNG with measurement positions indicated.

Fig. 30 compares calculated and measured neutron and photon spectra. It is found that FENDL-3.0 reproduces well the neutron spectra, in general better than FENDL-2.1. When comparing C/E ratios for the neutron fluxes, integrated over specific energy ranges, FENDL-3.0 is shown to be superior to FENDL-2.1, see Fig. 31. FENDL-3.0 also reproduces well the photon spectra although the fluxes above 5 MeV are slightly underestimated in comparison with FENDL-2.1.

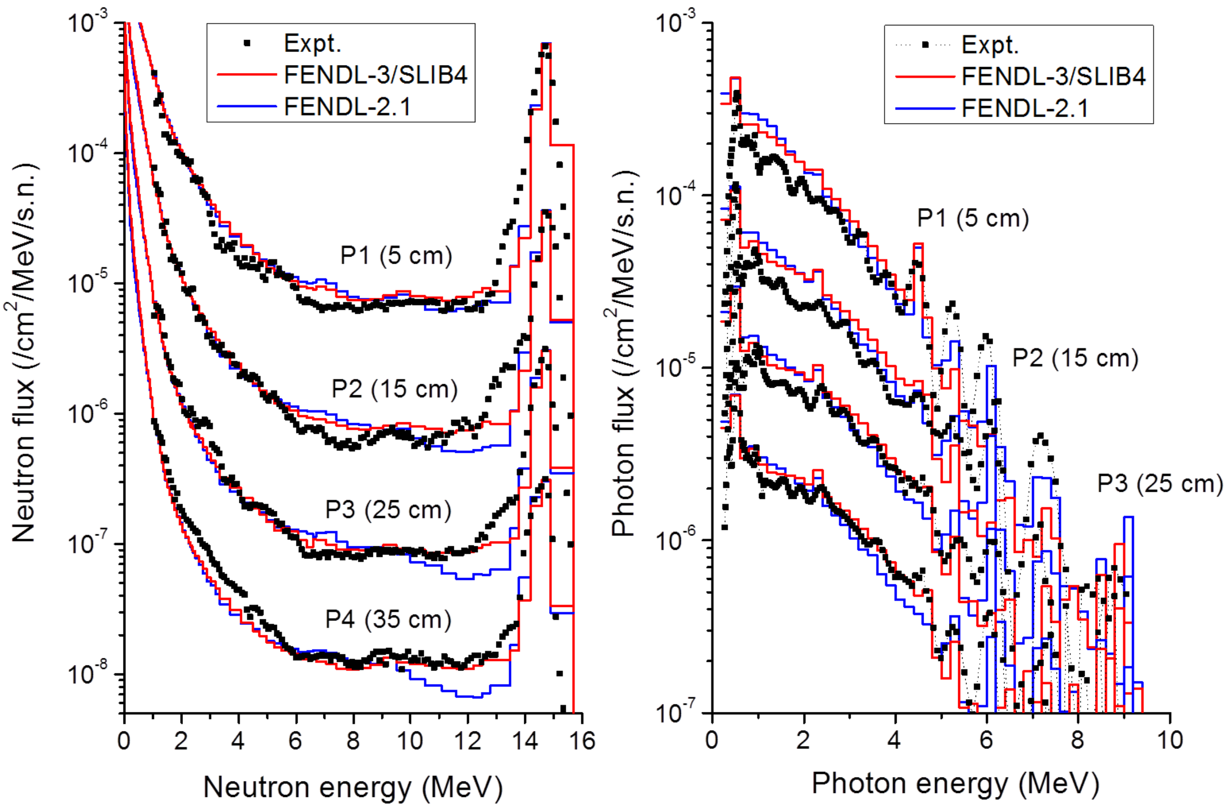

Fig. 30: Results obtained for the neutron (left) and photon (right) flux spectra at the four positions P1 – P4 (5, 15, 25, and 35 cm) in the W benchmark experiment at FNG.

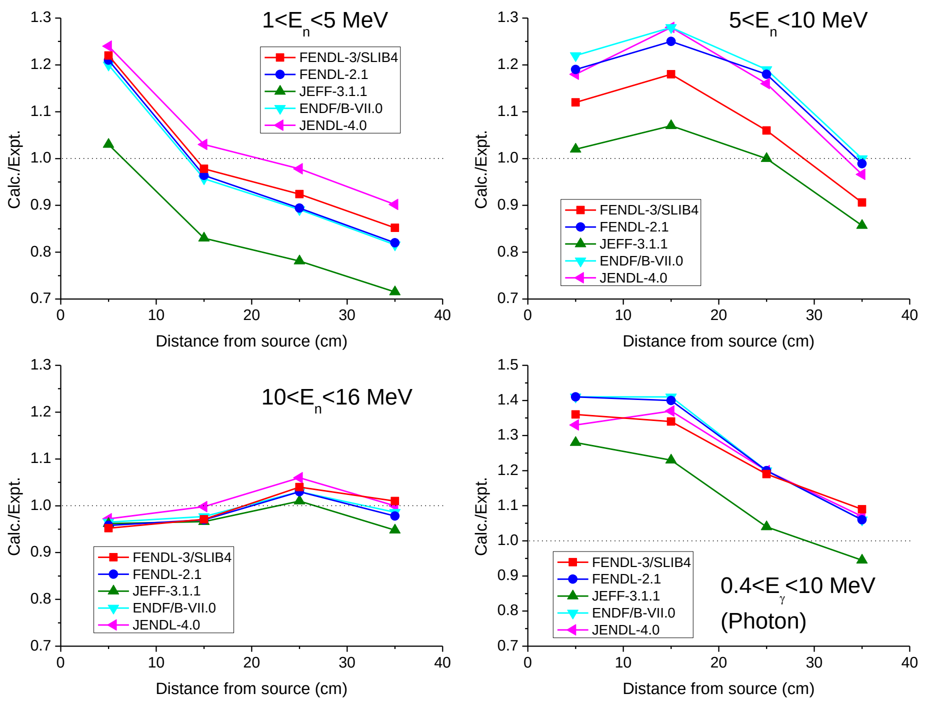

Fig. 31: C/E ratios for the neutron and photon flux spectra integrated over different energy ranges as obtained at the positions P1 – P4 (5, 15, 25, and 35 cm) for the W benchmark at FNG.

Tritium breeding validation experiments

Tritium breeding validation experiments were performed at FNG on neutronic mock-ups of the HCPB (Helium–Cooled Pebble Bed) and the HCLL Helium-Cooled Lithium Lead) Test Blanket Modules (TBM) which are under development in the EU for irradiation tests in ITER.

The neutronic **HCPB mock-up** [15] replicated the main characteristics of a breeder insert of the HCPB TBM in ITER consisting of a stainless steel box filled by alternating layers of breeder material (Li_2CO_3) and neutron multiplier (Be) separated by thin steel walls. The experiment included measurements of the tritium generated during irradiation in several Li_2CO_3 pellet stacks located at different penetration depths, measurements of various reaction rates using the activation foil technique, as well as measurements of fast neutron and photon flux spectra.

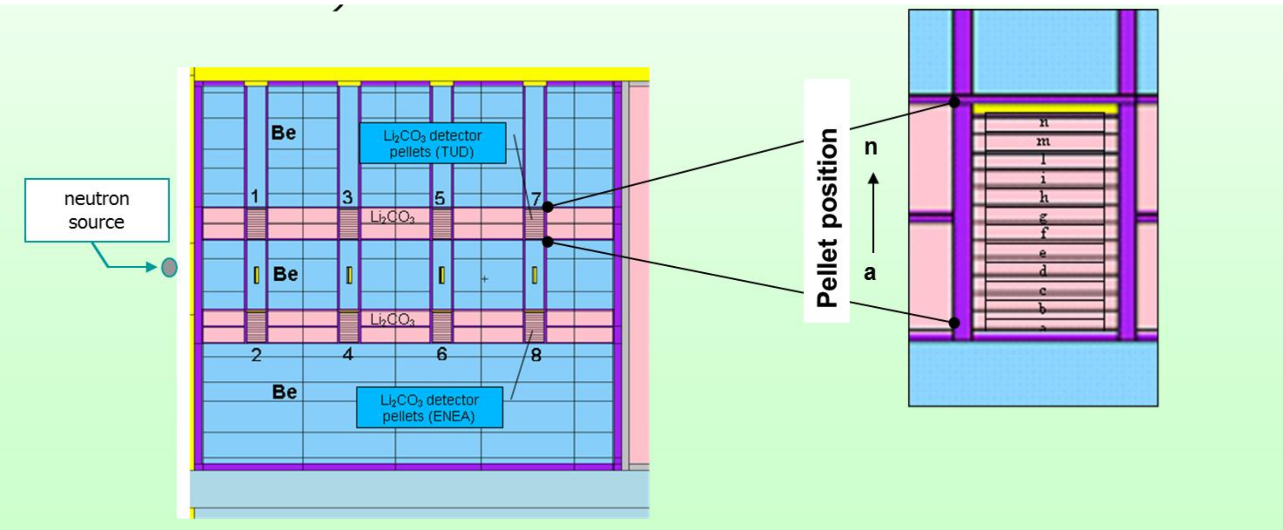

Fig. 32: Schematic set-up of the HCPB breeder blanket mock-up benchmark experiment at FNG with the pellet stacks for the tritium measurements and the positions of the activation foils (yellow) indicated.

Fig. 33 shows the C/E ratios for the reaction rates $^{197}Au(n,\gamma)\,^{198}Au$, $^{58}Ni(n,p)\,^{58}Co$, $^{58}Ni(n,2n)\,^{57}Ni$, and $^{93}Nb(n,2n)\,^{92}Nb$ as function of the penetration depth. It is noted that there is very good agreement between calculated and measured reaction rates within the experimental uncertainty. The FENDL-3.0 and FENDL-2.1 result agree in general. For the Nb-93(n,2n)Nb-92 reaction rate, which is sensitive to high energy neutrons, there is, however a noticeable trend for a small underestimation with increasing penetration depth.

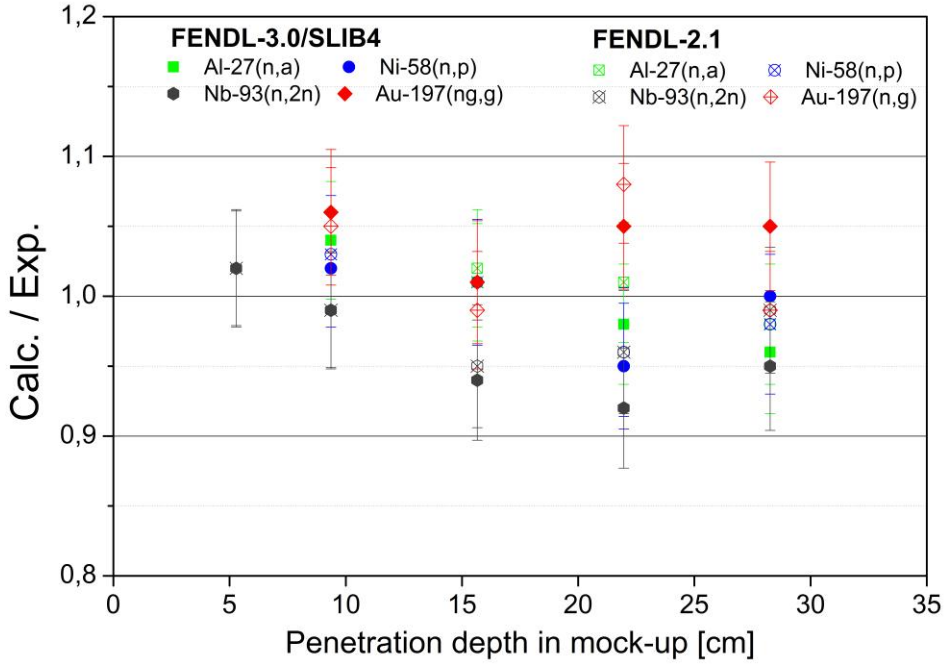

Fig. 33: C/E ratios for reaction rates measured in the HCPB mock-up experiment at FNG as function of the penetration depth (FENDL-3.0/SLIB4: closed symbols, FENDL-2.1: open symbols).

The tritium generated in the Li_2CO_3 pellets during irradiation was shown to be underestimated by 5 to 10% on average independent of the nuclear data used, see Fig. 34. This is also true for FENDL-3.0 with a slightly stronger trend for the underestimation (2 to 3% as compared with FENDL-2.1). A detailed investigation including the replacement of all FENDL-3 cross-sections by FENDL-2.1 - except those of Be - showed that the reduced tritium production is due to the different Be data employed in the calculations. No differences of the Be cross-section data in FENDL-3.0/SLIB4 and FENDL-2.1, originating from ENDF/B-VII.1 and ENDF/B-VI.8, respectively, were found except for the elastic scattering cross-sections displayed in Fig. 35. It was thus deduced that the small reduction of the scattering cross-section below some 0.2 MeV is causing the observed reduction of the tritium production. This is actually consistent with the results of the sensitivity analyses performed previously on the tritium production in the HCPB TBM mock-up experiment [16].

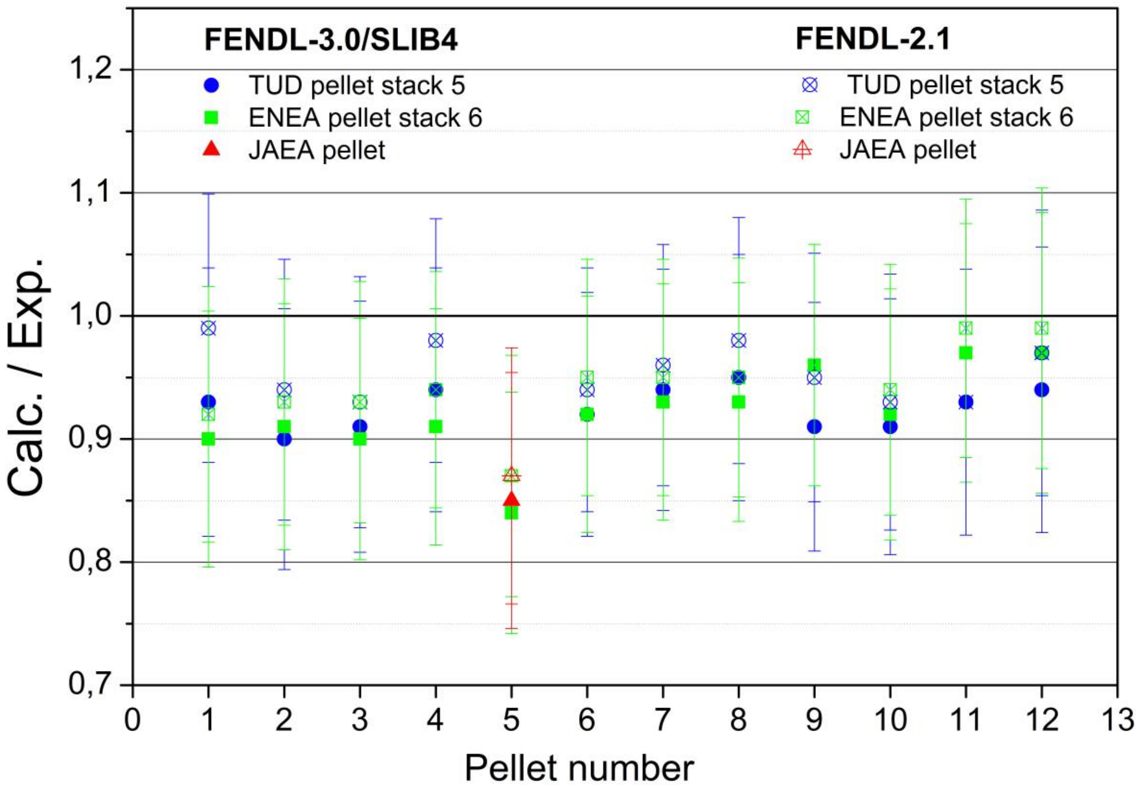

Fig. 34: C/E ratios for the tritium generated in selected Li_2CO_3 pellets in the HCPB mock-up experiment at FNG as function of the penetration depth (FENDL-3.0/SLIB4: closed symbols, FENDL-2.1: open symbols).

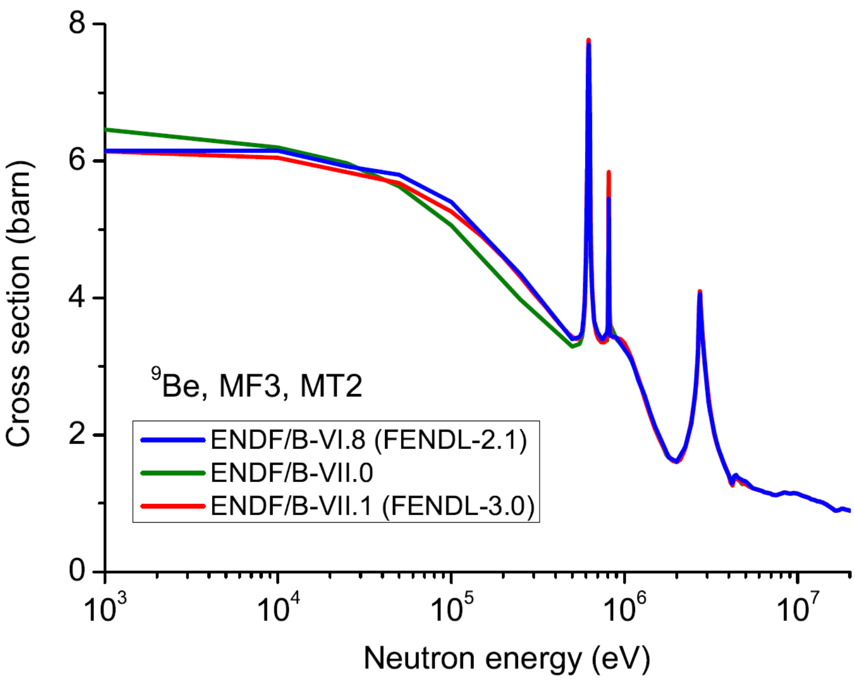

Fig. 35: Elastic scattering cross-section of Be-9 as function of neutron energy, as included in FENDL-2.1 (ENDF/B-VI.8), FENDL-3.0 (ENDF/B-VII.1) and ENDF/B-VII.0.

The neutronic **HCLL mock-up** [17] consisted of alternate layers of solid Pb-Li bricks and Eurofer steel plates. Two thin layers and a reflector of Polyethylene were introduced inside the mock-up and its back, respectively, to simulate the effect of neutron reflecting materials surrounding the TBM module in ITER. Again measurements were performed of the tritium produced in several Li_2CO_3 pellet stacks, of reaction rates and of neutron/ photon flux spectra. Fig. 36 shows the schematic set-up of the mock-up experiment.

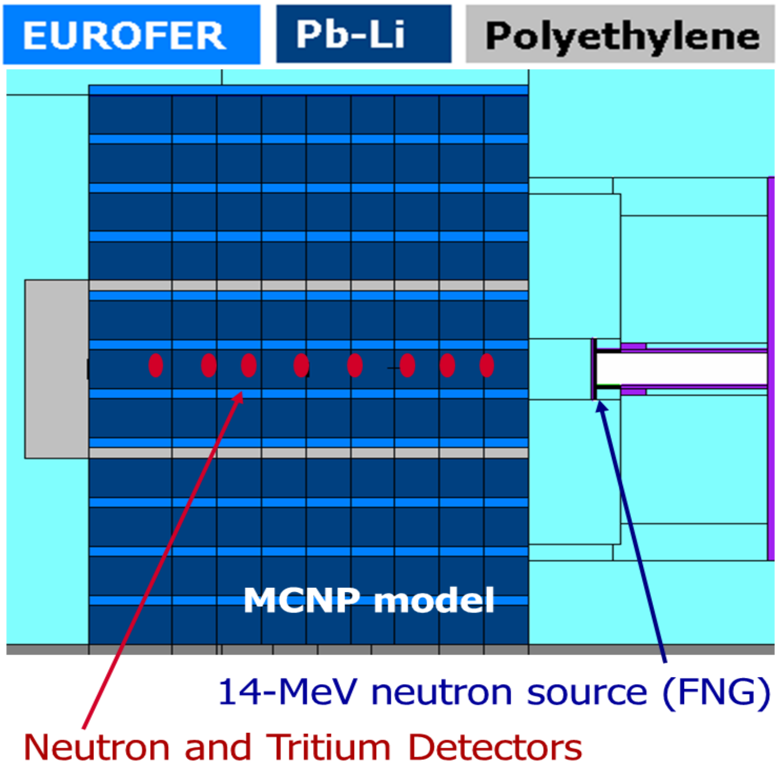

Fig. 36: Schematic set-up of the HCLL breeder blanket mock-up benchmark experiment at FNG with the tritium and activation foils measurement positions indicated.

There is again good agreement of the measured and calculated reaction rates, within the experimental uncertainties, both for FENDL-3.0 and FENDL-2.1, with the exception of the Ni-58(n,2n) reaction which is underestimated with FENDL-3.0 up to 10 – 15 %, see Fig. 37. This indicates an underestimation of the fast neutron flux in the HCLL TBM.

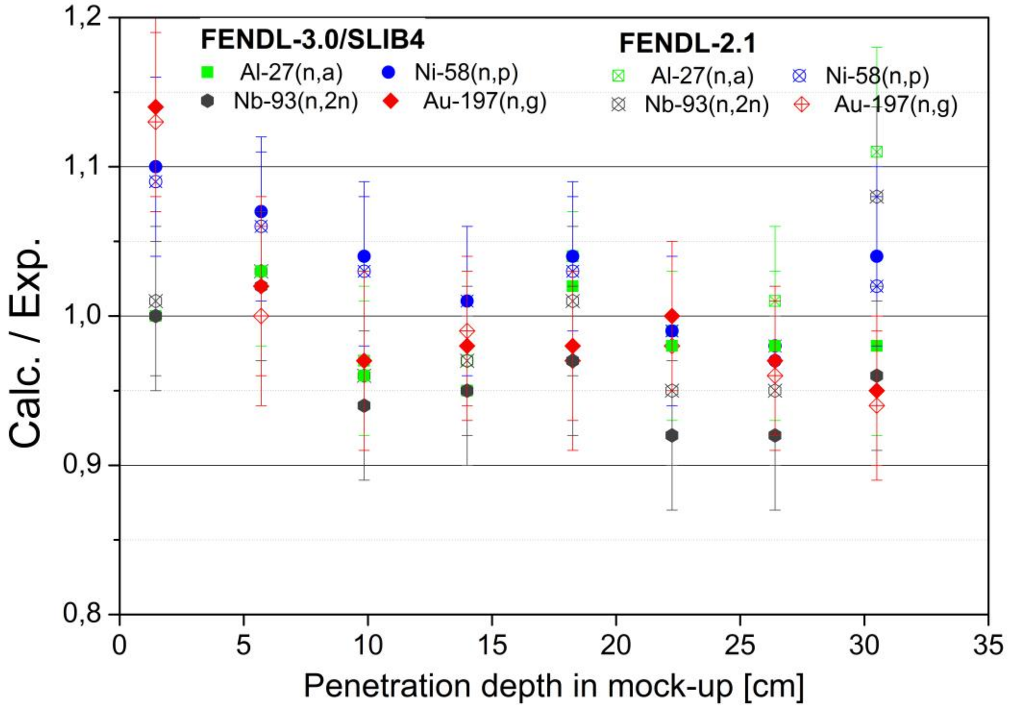

Fig. 37: C/E ratios for reaction rates measured in the HCLL mock-up experiment at FNG as function of the penetration depth (FENDL-3.0/SLIB4: closed symbols, FENDL-2.1: open symbols).

In case of the HCLL mock-up experiment, the tritium generated in the Li_2CO_3 pellets is well reproduced within the experimental uncertainty with all data libraries, see Fig. 38. There is just the exception of the tritium produced in the natural enriched Li_2CO_3 pellets in the rear of the mock-up which is underestimated by the calculations. This underestimation, however, is independent on the nuclear data used.

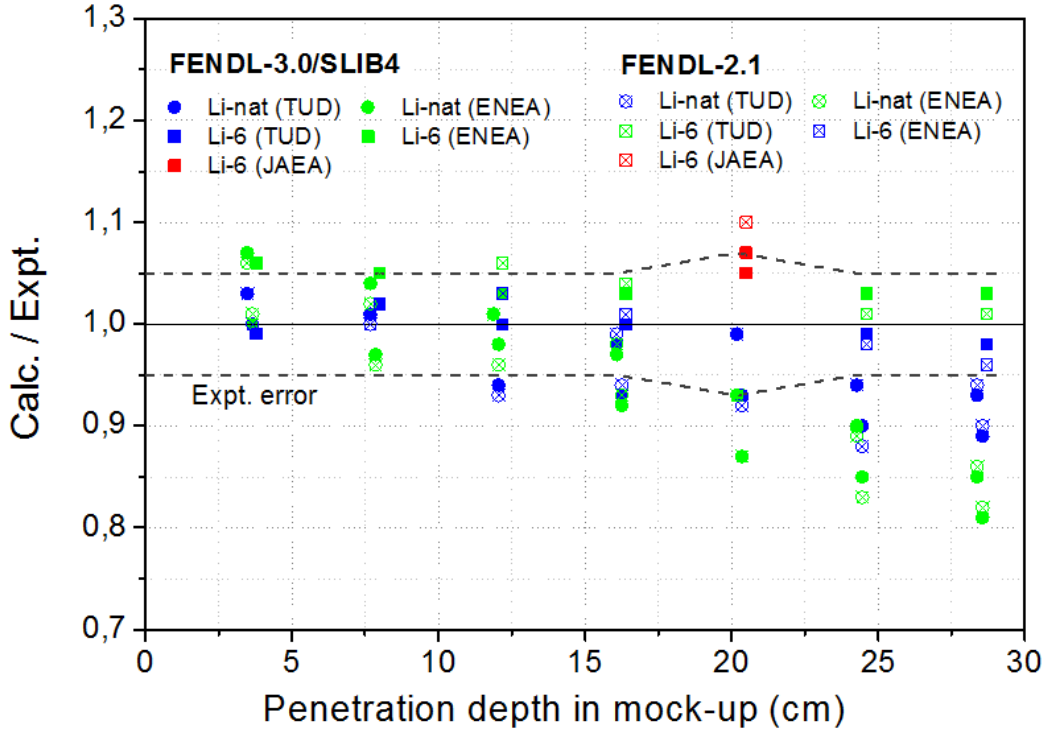

Fig. 38: C/E ratios for the tritium generated in selected Li_2CO_3 pellets in the HCLL mock-up experiment at FNG as function of the penetration depth (FENDL-3.0/SLIB4: closed symbols, FENDL-2.1: open symbols).

4.3 OKTAVIAN Benchmark Experiments

Leakage neutron spectra from spherical piles were measured with the time-of flight (TOF) technique at the DT neutron source facility OKTAVIAN in Osaka University [18]. The piles were made by filling spherical vessels with sample powder or flakes of CF_2, Al, Si, Ti, Cr, Mn, Co, Cu, Zr, Nb, Mo and W. DT neutrons were produced by bombarding a 370 GBq tritium target placed at the centre of the pile with 250 keV deuteron beam. A cylindrical liquid organic scintillator NE-218 was used as a neutron detector, which was located at about 11 m from the tritium target and 55 deg. with respect to the deuteron beam axis, surrounded by concrete or heavy concrete. A pre-collimator made of polyethylene-iron multi-layers was set between the pile and the detector in order to reduce the background neutrons. The experimental arrangement is shown in Fig. 39.

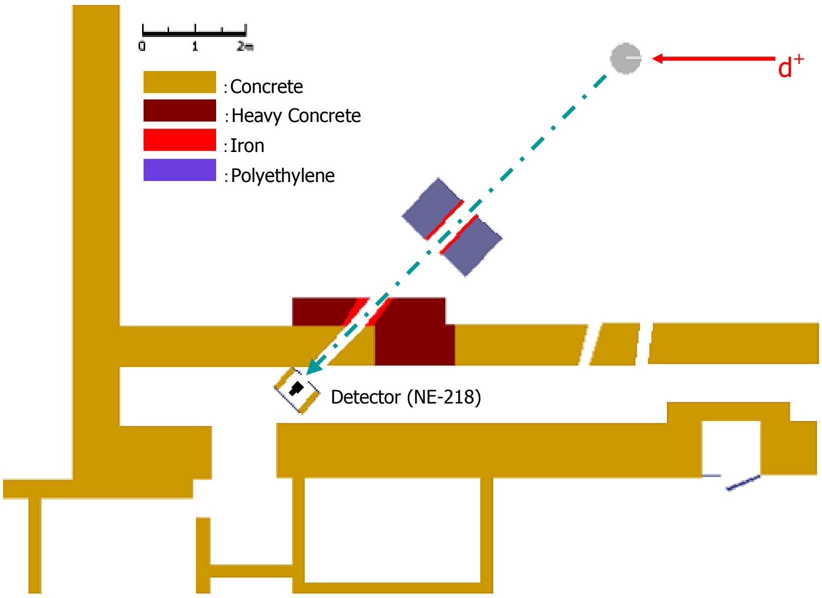

Fig. 39: Schematic set-up of the OKTAVIAN experiments.

All calculations were performed with the MCNP5 Monte Carlo code using the nuclear data libraries FENDL-2.1, FENDL-3/SLIB4, and, for comparison, the latest version of the Japanese Nuclear Data Library JENDL-4.0. Graphical results are displayed in Figs. 40 - 51. A brief discussion of the results is included in Table XII.

TABLE XII: SUMMARY OF OKTAVIAN BENCHMARK EXPERIMENTS – MATERIAL CONFIGURATIONS AND DISCUSSION OF RESULTS.

Material	Nominal outer diameter	Results discussion
Al	40 cm	The calculation results with FENDL-3 are slightly better than those with FENDL-2.1 and JENDL-4.
CF_2	40 cm	All the calculation results underestimate the measured ones. The measured data might include some errors.
Co	40 cm	The calculation results with FENDL-3 are the same as those with FENDL-2.1. The JENDL-4 results are better than those with FENDL-3 for neutrons from 4 to 11 MeV.
Cr	40 cm	The calculation results with FENDL-3 are better than those with FENDL-2.1 and JENDL-4 except for neutrons from 0.5 to 1 MeV for which FENDL-3 gives a larger overestimation.
Cu	61 cm	The calculation results with FENDL-3 are the same as those with FENDL-2.1. JENDL-4 gives better agreement than FENDL-3 for neutrons from 1 to 11 MeV.
Mn	61 cm	The calculation results with FENDL-3 are better than those with FENDL-2.1 for neutrons above 1 MeV. Worse agreement is obtained for neutrons below 1 MeV.
Mo	61 cm	The calculation results with FENDL-3 are better than those with FENDL-2.1 for neutrons from 0.5 to 10 MeV.
Nb	28 cm	The calculation results with FENDL-3 are better than those with FENDL-2.1 for neutrons below 1 MeV. Worse agreement is obtained for neutrons from 1 to 10 MeV.
Si	60 cm	The calculation results with FENDL-3 are the same as those with FENDL-2.1. JENDL-4 gives better agreement than FENDL-3 for neutrons below 10 MeV.
Ti	40 cm	The calculation results with FENDL-3 are better than those with FENDL-2.1 and JENDL-4 for neutrons below 1 MeV. Worse or the same agreement is obtained for neutrons above 1 MeV.
W	40 cm	The calculation results with FENDL-3 are almost the same as those with FENDL-2.1 and JENDL-4.
Zr	61 cm	All the calculation results are the same. They overestimate neutrons below 1 MeV.

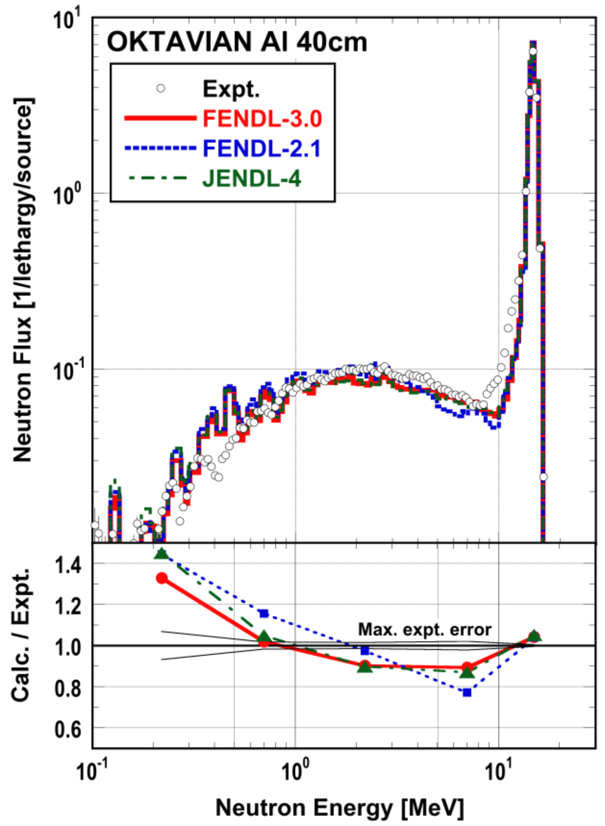

Fig. 40: Leakage neutron spectra from Al sphere.

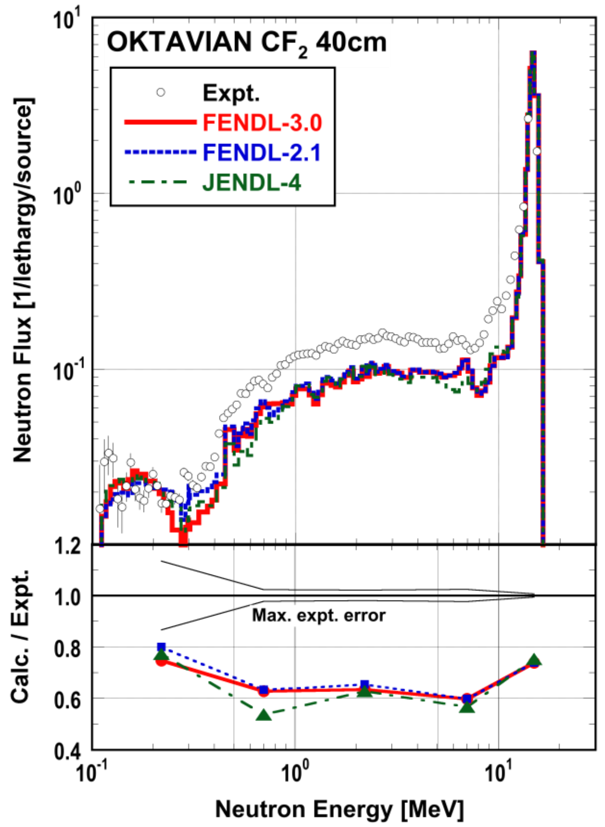

Fig. 41: Leakage neutron spectra from CF2 sphere.

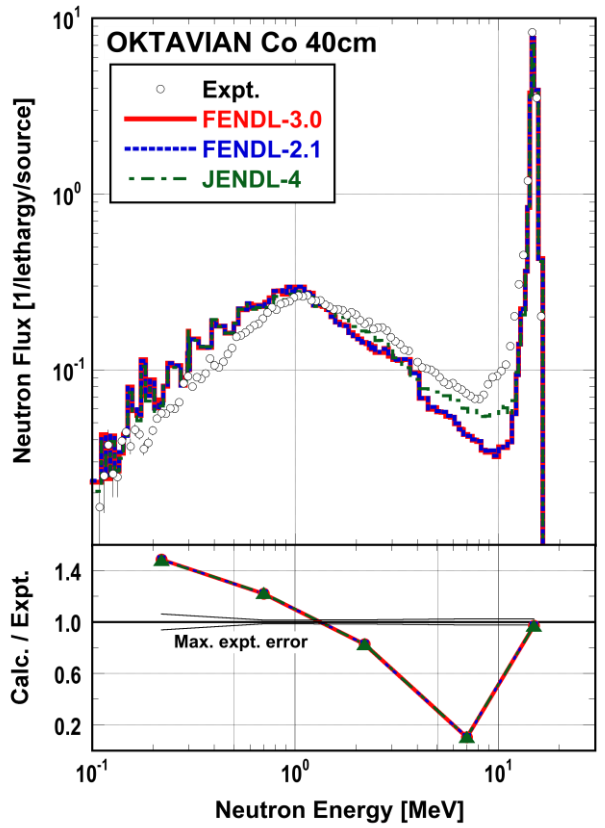

Fig. 42: Leakage neutron spectra from Co sphere.

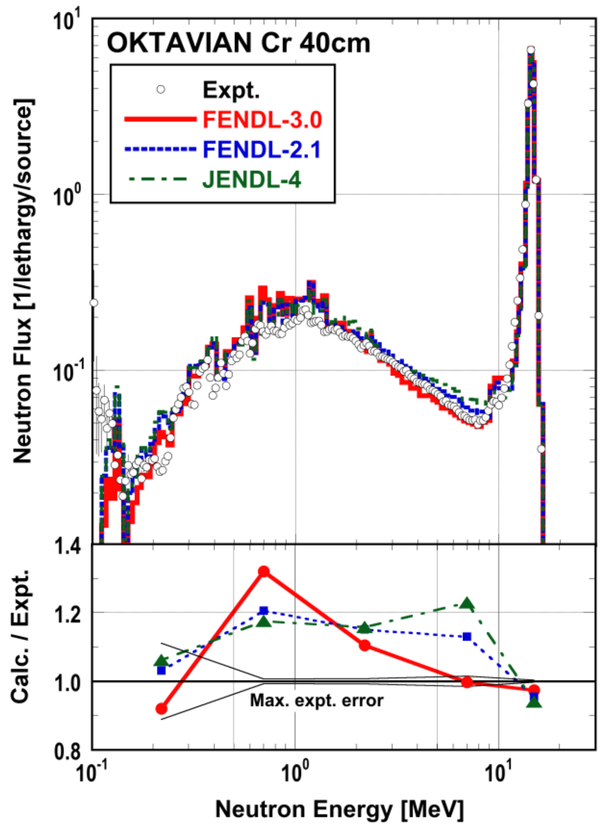

Fig. 43: Leakage neutron spectra from Cr sphere.

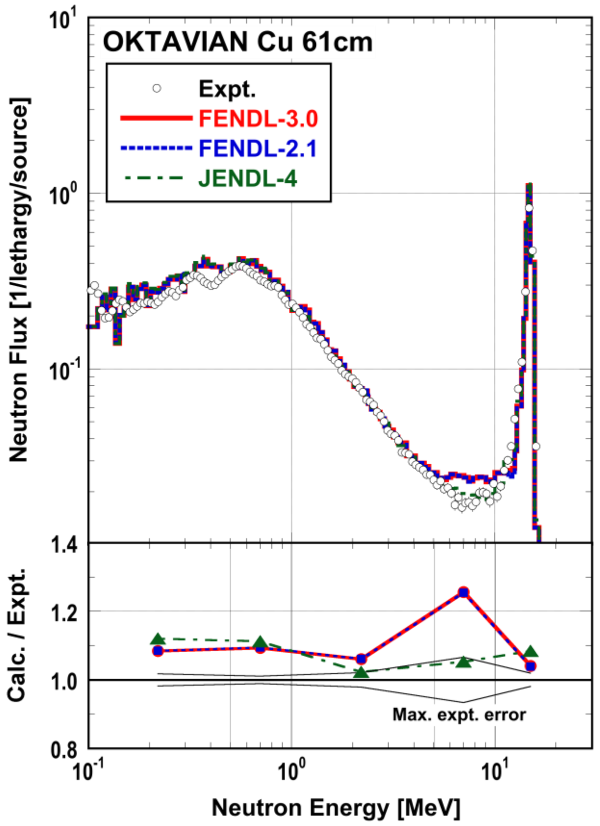

Fig. 44: Leakage neutron spectra from Cu sphere.

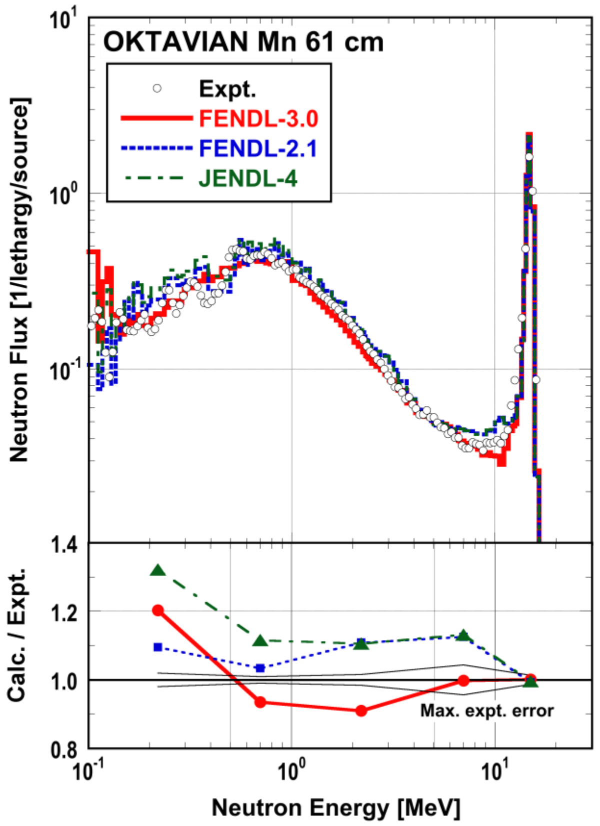

Fig. 45: Leakage neutron spectra from Mn sphere.

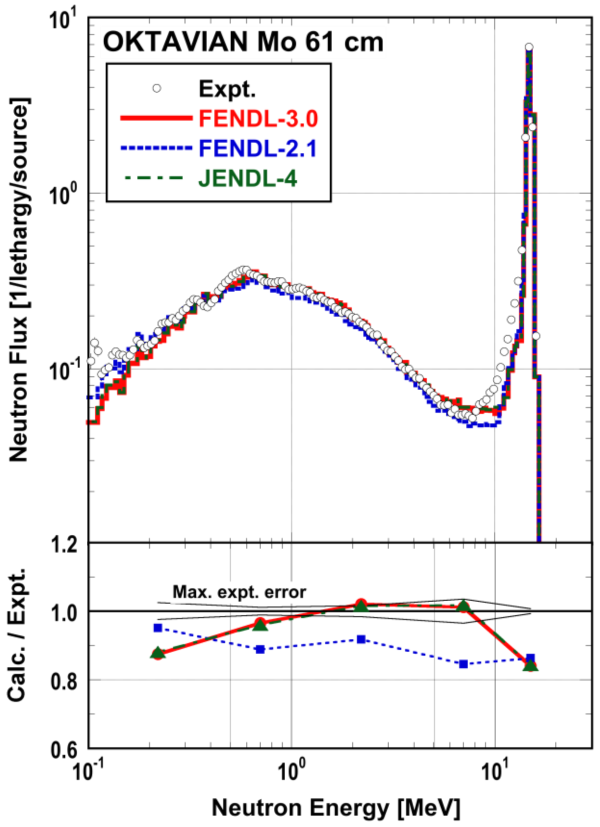

Fig. 46: Leakage neutron spectra from Mo sphere.

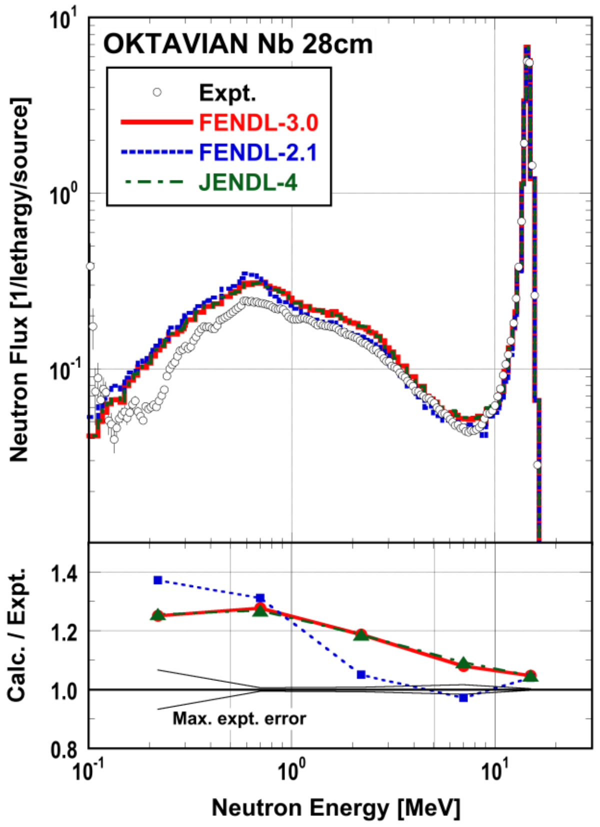

Fig. 47: Leakage neutron spectra from Nb sphere.

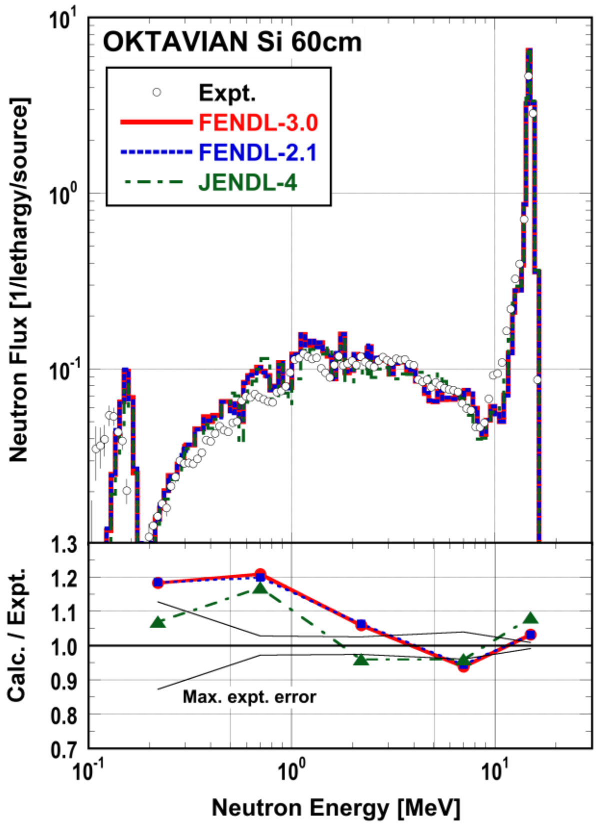

Fig. 48: Leakage neutron spectra from Si sphere.

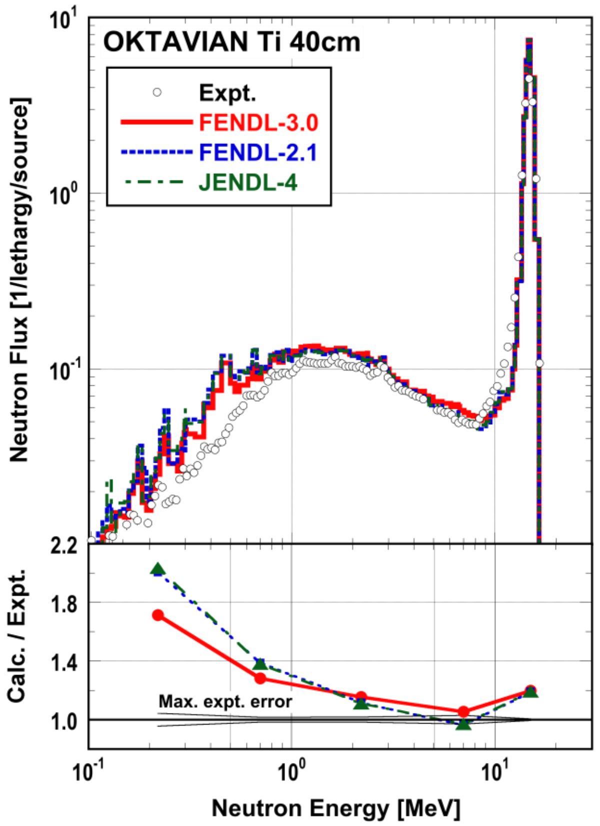

Fig. 49: Leakage neutron spectra from Ti sphere.

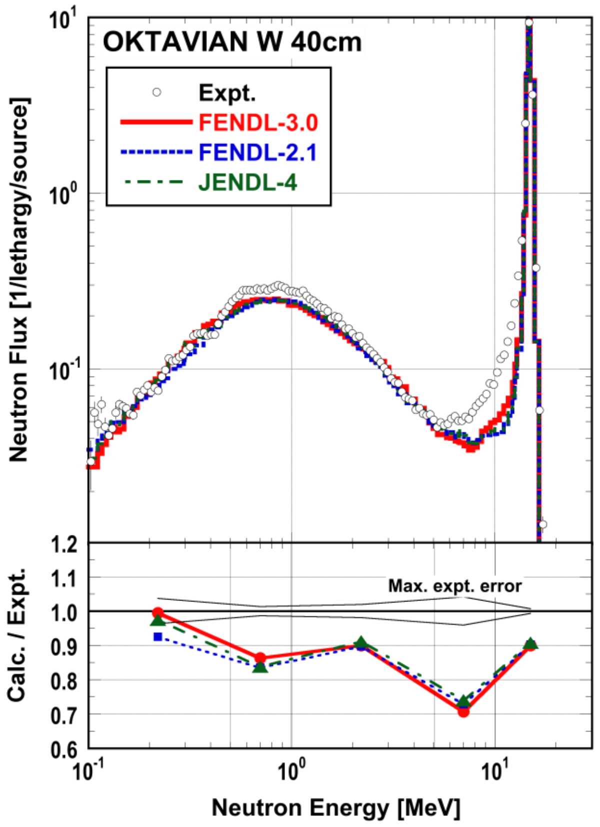

Fig. 50: Leakage neutron spectra from W sphere.

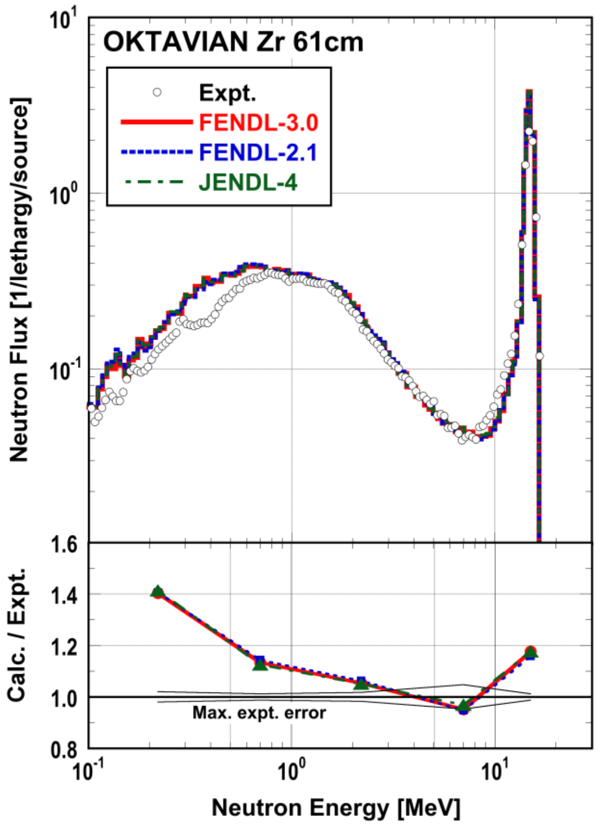

Fig. 51: Leakage neutron spectra from Zr sphere.

5. Conclusion

FENDL-3 benchmark analyses were performed on a computational ITER benchmark and a series of available 14 MeV neutron benchmark experiments. The computational benchmark revealed a modest increase of the neutron flux levels in the deep penetration regions and a substantial increase of the gas production in steel components. The comparison to experimental results showed good agreement with no substantial differences between FENDL-3.0 and FENDL-2.1 for most responses. There is a slight trend, however, for an increase of the fast neutron flux in the shielding experiment and a decrease in the breeder mock-up experiments. The photon flux spectra measured in the bulk shield and the tungsten experiments are significantly better reproduced with FENDL-3.0 data. In general, FENDL-3, as compared to FENDL-2.1, shows an improved performance for fusion neutronics applications. It is thus recommended to ITER to replace FENDL-2.1 as reference data library for neutronics calculation by FENDL-3.0.

6. References

[1] V. Goulo, FENDL, Proceedings of the IAEA Specialists' Meeting on Fusion Evaluated Nuclear Data Library (FENDL), INDC(NDS)-223 (1989).

[2] D. Lopez Aldama, A. Trkov, FENDL-2.1, Update of an Evaluated Nuclear Data library for Fusion Applications, INDC(NDS)-467 (2004).

[3] http://www.iter.org.

[4] R. A. Forrest *et al.*, FENDL-3 Summary documentation, INDC(NDS)-628 (2013).

[5] P. Garin, M. Sugimoto, Fusion Eng. and Des. **84**, (2009) 259.

[6] http://www.iaea-nds.iaea.org/fendl30/.

[7] X-5 Monte Carlo Team, LA-UR-03-1987, Los Alamos National Laboratory (April, 24, 2003).

[8] M. Sawan, FENDL Neurtonics Benchmark: Specifications for the Calculational Neutronics and Shielding Benchmark, INDC(NDS)-316 (1994).

[9] SINBAD FUSION, NEA-1553, http://www.oecd-nea.org/tools/abstract/detail/NEA-1552.

[10] F. Maekawa, C. Konno, Y. Kasugai, Y. Oyama, Y. Ikeda, Data Collection of Fusion Neutronics Benchmark Experiment Conducted at FNS/JAEA, JAERI-Data/Code 98-021 (1998) *et al.*, JAERI-Data/Code 98-021 (1998).

[11] Y. Oyama, S. Yamguchi, H. Maekawa, Experimental results of angular neutron flux spectra leaking from slabs of fusion reactor candidate materials, I, JAERI-M 90-092 (1990).

[12] K. Shibata *et al.*, JENDL-4.0: A New Library for Nuclear Science and Engineering, J. Nucl. Sci. Technol. **48**, (2010) 1.

[13] P. Batistoni *et al.*, Neutronics experiment on a mock-up of the ITER shielding blanket at the Frascati Neutron Generator, Fusion Eng. Des. **47** (1999) 25.

[14] P. Batistoni *et al.*, Neutronics benchmark experiment on tungsten, Journal of Nuclear Materials, **329–333**, Part A (2004) 683.

[15] P. Batistoni *et al.*, Neutronics Experiment on a Helium Cooled Pebble Bed (HCPB) Breeder Blanket Mock-up, Fusion Eng. and Des. **82**(2007) 2095.

[16] D. Leichtle *et al.*, Sensitivity and Uncertainty Analyses of the Tritium Production in the HCPB Breeder Blanket Mock-up Experiment, Fusion Eng. Des. **82** (2007) 2407.

[17] P. Batistoni *et al.*, Neutronics Experiments on HCPB and HCLL TBM Mock-ups in Preparation of Nuclear Measurements in ITER, Fusion Eng. Des. **85** (2010) 1675.

[18] F. Maekawa, J. Yamamoto, C. Ichihara, K. Ueki, Y. Ikeda, Collection of experimental data for fusion neutronics benchmark, JAERI-M 94-014 (1994).

Nuclear Data Section
International Atomic Energy Agency
Vienna International Centre, P.O. Box 100
A-1400 Vienna, Austria

E-mail: nds.contact-point@iaea.org
Fax: (43-1) 26007
Telephone: (43-1) 2600 21725
Web: http://www-nds.iaea.org